The Astronomical Journal, 161:88 (20pp), 2021 February https://doi.org/10.3847/1538-3881/abd18c

Parsec-scale Properties of Steep- and Flat-spectrum Extragalactic Radio Sources from a VLBA Survey of a Complete North Polar Cap Sample

A. V. Popkov[1,2], Y. Y. Kovalev[1,2,3], L. Y. Petrov[4], and Yu. A. Kovalev[2]
[1] Moscow Institute of Physics and Technology, Institutsky per. 9, Dolgoprudny 141700, Russia; popkov.av@mipt.ru
[2] Astro Space Center of Lebedev Physical Institute, Profsoyuznaya 84/32, 117997 Moscow, Russia
[3] Max-Planck-Institut für Radioastronomie, Auf dem Hügel 69, D-53121 Bonn, Germany
[4] NASA Goddard Space Flight Center, 8800 Greenbelt Rd., Greenbelt, MD 20771, USA
Received 2020 August 15; revised 2020 November 17; accepted 2020 November 26; published 2021 January 28

Abstract

We observed with the Very Long Baseline Array (VLBA) at 2.3 and 8.6 GHz a complete flux-density-limited sample of 482 radio sources with decl. $> +75°$ brighter than 200 mJy at 1.4 GHz drawn from the NVSS catalog. A total of 34% of the sources show parsec-scale emission above the flux density detection limit of 30 mJy; their accurate positions and parsec-scale structure parameters are determined. Among all the sources detected at least at the shortest VLBA baselines, the majority, or 72%, have a steep single-dish spectrum. The fraction of the sources with a detectable parsec-scale structure is above 95% among the flat-spectrum objects and close to 25% among the steep-spectrum objects. We identified 82 compact steep-spectrum source candidates, which make up 17% of the sample; most of them are reported for the first time. The compactness and the brightness temperature of the sources in our sample show a positive correlation with single-dish and VLBA spectral indices. All the sources with a significant 8 GHz variability were detected by the VLBA snapshot observations, which independently confirmed their compactness. We demonstrated that 54% of the sources detected by the VLBA at 2.3 GHz in our sample have a steep VLBA spectrum. The compact radio emission of these sources is likely dominated by optically thin jets or mini-lobes, not by an opaque jet core. These results show that future VLBI surveys aimed at searching for new sources with parsec-scale structure should include not only flat-spectrum sources but also steep-spectrum ones in order to reach an acceptable level of completeness.

Unified Astronomy Thesaurus concepts: Galaxy jets (601); Active galactic nuclei (16); Radio astrometry (1337); Radio astronomy (1338); Radio continuum emission (1340); Radio sources (1358); Very long baseline interferometry (1769); Radio interferometry (1346)

Supporting material: figure set, machine-readable tables

1. Introduction

Over the past decades, more than a dozen large-area surveys of active galactic nuclei (AGNs) have been carried out using very long baseline interferometry (VLBI). These surveys include, among others, Preston et al. (1985), the series of the Very Long Baseline Array (VLBA) Calibrator Surveys (Beasley et al. 2002; Fomalont et al. 2003; Petrov et al. 2005, 2006; Kovalev et al. 2007; Petrov et al. 2008; Gordon et al. 2016), the VLBA Imaging and Polarimetry Survey (Helmboldt et al. 2007), the LBA Calibrator Surveys (Petrov et al. 2011b, 2019a), and the VLBA Galactic Plane Survey (Petrov et al. 2011a). Due to the narrow field of view, typically 1–10″, VLBI surveys usually follow up the objects detected with low-resolution connected-element interferometry or single-dish observations. It was found that if one were to take a flux-density-limited sample of flat-spectrum extragalactic sources and follow them up with VLBI, most of them would be detected (e.g., Pearson & Readhead 1981; Preston et al. 1985; Taylor et al. 1996; Petrov et al. 2005, 2006; Kovalev et al. 2007), up to 90%. The reason for that is the presence of the opaque VLBI core, which typically has a flat spectrum and dominates the total emission of flat-spectrum AGNs (e.g., Kovalev et al. 2005; Pushkarev & Kovalev 2012; Hovatta et al. 2014). We classify a source spectrum as flat if its flux density dependence on frequency ν is described by the power law $S(\nu) \propto \nu^{+\alpha}$ with the spectral index $\alpha \geqslant -0.5$. Since the goal of the surveys was to provide a dense grid of calibrators using minimum resources, the source selection algorithm was tuned to maximize the number of detections. Therefore, these surveys targeted almost exclusively flat-spectrum sources. As a result, VLBI catalogs have a heavy bias toward flat-spectrum sources. Their dominance in VLBI catalogs prompted researchers to consider them to belong to a special class: compact AGNs.

But then a question arises about the nature of steep-spectrum sources ($\alpha < -0.5$) that make up about 90% of extragalactic radio sources brighter than 200 mJy at 1.4 GHz (Mingaliev et al. 2007): Are they different? Do steep-spectrum sources belong to the same population as flat-spectrum sources, or do they form a distinctive population? Steep-spectrum sources remain poorly studied at parsec scales. Experience from the surveys mentioned above has shown that they are often heavily resolved by VLBI. At the same time, a number of compact steep-spectrum (CSS) sources have been found and studied by VLBI (e.g., Marecki et al. 2006; Kunert-Bajraszewska & Marecki 2007; Dallacasa et al. 2013; Collier et al. 2018). O'Dea (1998) defines CSS sources as those with steep spectra in centimeter range and sizes $\leqslant$20 kpc. How many extragalactic steep-spectrum sources have VLBI-compact structures? More generally, what fraction of the whole AGN population has observable parsec-scale jets? Therefore, how many sources are missed by VLBI surveys limited to flat-spectrum targets?

To address these questions, one needs a VLBI survey of a statistically complete, unbiased sample. To date, very few such surveys have been made. Giovannini et al. (2005) and Liuzzo et al. (2009) presented the results of the VLBI observations of the Bologna Complete Sample (BCS) of 76 objects selected

from the low-frequency B2 catalog (408 MHz) and 3CR catalog (178 MHz). Their sample is flux density limited with a completeness of 80% but includes only sources with redshift $z < 0.1$. With a sufficiently low detection limit (5 mJy at 5 GHz), they detected using VLBI 96% of the observed sources, which means that most of the sources have compact radio nuclei. The combination of Pearson-Readhead and Caltech-Jodrell Bank VLBI surveys (PR+CJ1; Pearson & Readhead 1981, 1988; Polatidis et al. 1995; Thakkar et al. 1995; Xu et al. 1995) formed another statistically complete sample of 200 objects with total flux density at an intermediate frequency of 5 GHz $S_{5\mathrm{GHz}} > 0.7$ Jy, covering 20% of the sky. Two-thirds of the sources have been detected and imaged with VLBI at 1.6 and 5 GHz. Among 65 sources of this sample with $S_{5\mathrm{GHz}} > 1.3$ Jy, the authors found 10 compact sources with a steep spectrum. Chhetri et al. (2013) analyzed the distribution of the ratio of visibility amplitudes at long (4.5 km) and short (200 m) ATCA baselines and its relation to the spectral index for 5539 sources from the AT20G catalog (Murphy et al. 2010) at 20 GHz. Among these sources, 27% are steep-spectrum objects. For most flat-spectrum sources, the visibility amplitude decreases by less than 15% between these baselines, which indicates that their angular size is less than $0\farcs15$. These authors also found that the share of sources with size less than 1 kpc and with a steep spectrum in the 1−4.8 GHz range is about 11% in their sample.

The mJIVE-20 survey (Deller & Middelberg 2014) and the deep VLBI surveys of the COSMOS (Herrera Ruiz et al. 2017) and GOODS-N (Radcliffe et al. 2018) fields utilized the phase referencing technique and covered small fields, 200, 2, and 0.5 deg^2, respectively. They observed all known AGNs at 1.4 GHz down to the surface brightness of 1 and 0.1 mJy beam^{-1}, respectively. There was no bias to flat-spectrum sources in these surveys. At the same time, they lack bright sources owing to the small size of the field.

All these works highlighted the necessity to have a systematic study of parsec-scale properties of the entire population of radio sources, not only a subsample of flat-spectrum objects. To address this need, we observed a large, complete, total flux-density-limited sample with the VLBA and analyzed the relations between the parsec-scale structure and the total simultaneous broadband radio spectra. This research has several goals: (i) to determine the share of compact objects among flat-spectrum and steep-spectrum radio sources; (ii) to determine the fraction of the VLBI-detected sources in a total flux-density-limited sample selected at 1.4 GHz; and (iii) to investigate parsec-scale properties of the VLBI-detected sources with a steep total spectrum, in particular, to understand whether they are mostly flat-spectrum cores of extended steep-spectrum sources or CSS sources. A systematic study of these problems is needed not only for understanding the physics of the AGN population and characterization of CSS sources but also for planning future VLBI observations and constructing VLBI-selected complete samples. The latter is critical for many applications, including the modern multimessenger neutrino-AGN VLBI studies (Plavin et al. 2020).

The paper is structured as follows. In Section 2, we define the sample and describe the VLBA observations. In Sections 3 and 4, we dwell on the VLBA data calibration and analysis procedure. We present the results of our survey in Section 5. Our RATAN-600 monitoring program, as well as the source spectra taken from the literature, are described in Section 6. We show the results of our joint analysis of the VLBA data and the continuum radio spectra in Section 7. We discuss the results in Section 8 and summarize them in Section 9.

Table 1
Observing Sample and the VLBA Detection Results

NVSS Name (1)	J2000 Name (2)	B1950 Name (3)	Det2 (4)	Det8 (5)
J001311+774846	J0013+7748	0010+775	Y	N
J033021+763323	J0330+7633	0324+763	N	Y
J170524+775559[c]	J1705+7756	1707+779	Y	Y
J190653+810010[a]	J1906+8100	1911+809	N	N
J190731+810008[a]	J1906+8100	1911+809	N	N

Notes. Column (1): source name in the NVSS catalog. Column (2): J2000 object name. Column (3): B1950 object name. Column (4): "Y" if a source was detected at 2.3 GHz in our VLBA survey and "N" otherwise. Column (5): same as Column (4), but for 8.6 GHz.
[a] The NVSS source is a component of an extended complex object. For all the components of each complex object, the same J2000 and B1950 names are given. These names correspond to the compact source detected by the VLBA, or, if the object was not detected, to the brightest of the NVSS components.
[b] The NVSS source is a component of an extended complex object, but the other components of this complex object are too weak to be included in our sample.
[c] The sources for which our J2000 name differs from the shortened NVSS name owing to the coordinate correction; see Section 2 for details.
(This table is available in its entirety in machine-readable form.)

2. Observing Sample and VLBA Observations

For our observations, we selected a sample of sources from the NVSS catalog (Condon et al. 1998), which meet the following criteria: (i) flux density $S_{\mathrm{NVSS}} \geqslant 200$ mJy at 1.4 GHz (NVSS frequency), (ii) decl. $\geqslant +75°$. The specific choice of the sky area and the flux density cutoff was dictated by the amount of VLBA observing time and recording bit rate we were able to secure. The north polar cap area was chosen for two reasons: it is always observable at all VLBA stations, and there are published broadband radio spectra for all the sources with $S_{\mathrm{NVSS}} \geqslant 200$ mJy within this area (see Section 6). There are 502 NVSS sources that satisfy these conditions, including two sources with $S_{\mathrm{NVSS}} = 199.9$ mJy. They are listed in Table 1. We named our program the VLBA North Polar Cap Survey (NPCS). Many studies (e.g., Condon et al. 2013; Kellermann et al. 2016; Padovani 2016, and the references therein) showed that AGNs dominate over star-forming galaxies among extragalactic radio sources with centimeter flux density higher than about 1 mJy. We assume, therefore, that all the sources in our sample are AGNs since they are much stronger.

Only a small fraction of the sources from our sample optical identifications are known. We searched for them in the NASA/IPAC Extragalactic Database (NED; Madore et al. 1992).[5] The optical types are available for 38 sources. There are 7 objects of the BL Lac type, 13 QSOs, and 18 radio galaxies, of which 6 sources belong to Seyfert 1 type and 6 sources belong to the Seyfert 2 type. There are redshift values in the NED for 41 sources from our sample. They are distributed from 0.003 to 3.4 with a median of about 0.6.

Some sources from this sample form pairs and groups. Namely, 36 sources have at least one other source from the sample at a

[5] https://ned.ipac.caltech.edu/

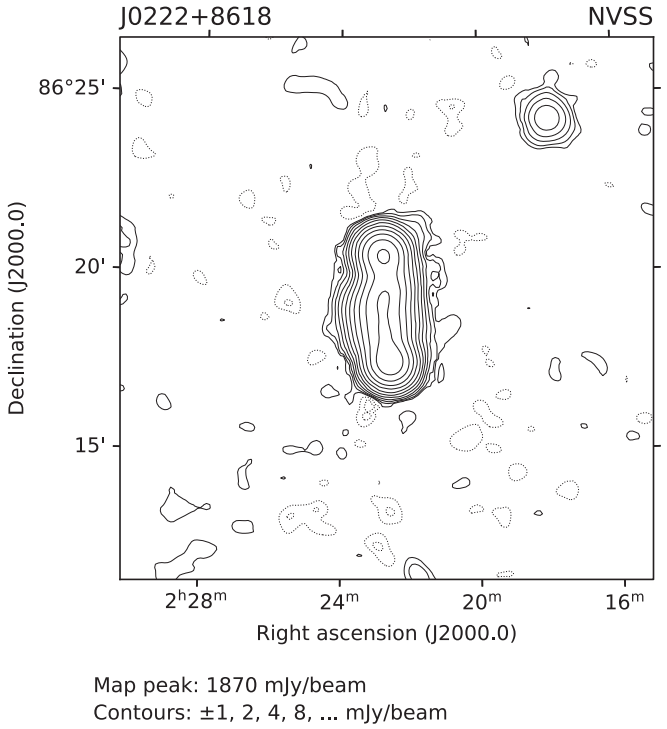

Figure 1. NVSS map for the complex source J0222+8618. The contours are plotted starting at 1 mJy beam^{-1} intensity level with an increment of 2.
(The complete figure set (22 images) is available.)

distance less than 4′. At the same time, if 502 sources of the sample were randomly scattered over 703 deg^2 of the considered area of the celestial sphere, we would expect only five sources with such close neighbors. This is evidence that among close pairs and goups, the majority are not apparently close separate sources, but are large extended sources resolved by the VLA to two or more components. The value of the distance limit of 4′ was found empirically; it seems to be optimal to distinguish extended resolved sources from individual apparently close sources in our sample. For this reason, we consider pairs/groups formed by these 36 sources as single sources and label each pair/group by one joint name. We also consider the source NVSS J204209 +751226 as a component of the complex source J2042+7508, because the NVSS map shows that it is indeed a component of this giant radio galaxy, although its distance to the closest neighbor is slightly larger than 4′. In total, there are 17 complex objects in the sample, consisting of 37 NVSS sources. Therefore, the actual number of sources in the sample is 482. The complex sources are marked in Table 1 by the label "*a*." Searching for the NVSS sources forming our sample in the NED and subsequent visual inspection of the NVSS images showed that five additional NVSS sources may be resolved components of extended complex galaxies. Other components of these complex sources are below our flux density cutoff of 200 mJy. These NVSS sources are marked in Table 1 by the label "*b*." In Figure Set 1, we show the NVSS maps for all 22 complex sources with at least one component belonging to our sample. The FITS images were obtained using the NVSS Postage Stamp Server.[6]

For several sources from our sample, the difference between the coordinates of the compact feature detected by the VLBA (see Table 2) and those of the centroid of the NVSS image results in the difference in the source names formed from these coordinates. These sources are marked in Table 1 by the label "*c*."

We observed this sample with the VLBA in three 24 hr observing sessions: on 2006 February 14, 16, and 23 (project code BK130). The telescopes were pointed to each of the 502 original NVSS sources. Each source was observed for about 8 minutes simultaneously in two frequency bands: 2.3 GHz (S band) and 8.6 GHz (X band), with single (right circular) polarization. Four 8 MHz wide intermediate frequencies (IFs) were allocated at each band. They cover 148 and 498 MHz at 2.3 and 8.6 GHz bands, respectively. With 1-bit sampling, the data bit rate was 64 Mbit s^{-1} in each band and 128 Mbit s^{-1} in total. In addition to the target sources, we also observed tropospheric calibration sources in eight blocks each day evenly distributed in time; each block consisted of four to five sources with different elevations; the calibration source scan duration was 90 s. Three sources from the sample (J0017+8135, J1058+8114, J1153 +8058) also served as calibrators. They were observed in two to three 90 s scans each day of the observations, in addition to an 8-minute scan on one of the days.

3. VLBA Data Processing

The data were correlated at the VLBA correlator at the NRAO Array Operations Center in Socorro. The correlator integration time was 0.5 s, and there were 64 spectral channels of width 125 kHz within each IF. This relatively high temporal and spectral resolution was necessary for fringe fitting with poorly known a priori coordinates, taken for most of the target sources from the NVSS catalog.

The data a priori calibration was made independently with two software packages: AIPS (Greisen 2003) and PIMA (Petrov et al. 2011a). These packages have different important advantages. Antenna-based fringe fitting is well implemented in AIPS. Additionally, the AIPS a priori amplitude calibration and bandpass normalization are extensively tested to deliver no significant amplitude bias. In turn, PIMA is capable of finding joint baseline-based fringe fitting solutions for frequency channels widespread around the band. It also precisely estimates the noise level of fringe solutions and the probability of a false detection. We explored the agreement between the results delivered by the two totally independent software packages. In both packages, all usual steps of calibration of the VLBI data were made, including (i) data flagging, (ii) a priori amplitude calibration, (iii) phase calibration using pulse-cal signal, (iv) fringe fitting, (v) complex bandpass calibration, and (vi) global antenna gain corrections derived from the self-calibration of the strongest sources.

3.1. A Priori Calibration and Detection Filter in PIMA

PIMA independently processes data collected from a given scan at a given baseline and a given band, hereafter called an observation. The procedure of fringe fitting determines the phase delay rate, the group delay, and the group delay rate using the spectrum of the cross-correlation function (also known as visibility data) across the band. See Petrov et al. (2011a) for details of this procedure implementation. The point-like source model is implicitly assumed in the procedure. The fringe fitting results were used in two ways. First, the group delays were used for our astrometric analysis. Second, the group delays, the phase delay rates, and the group delay

[6] https://www.cv.nrao.edu/nvss/postage.shtml

Table 2
J2000.0 Coordinates Measured for All the Sources Detected in the VLBA NPCS Survey, Including 162 Sources from the Target Sample and 4 Additional Sources

Name (1)	R.A. (2)	Decl. (3)	R.A. error (4)	Decl. Error (5)	Correlation (6)	Bands (7)
J0009+7724	00:09:43.09202	+77:24:42.00489	6.80	3.30	−0.322	XS
J0009+7603	00:09:48.23409	+76:03:18.16477	14.84	10.27	−0.498	XS
J0013+7748	00:13:11.70860	+77:48:46.67715	131.78	49.91	0.556	S
J0017+8135	00:17:08.47491	+81:35:08.13646	1.17	0.21	−0.023	XS
J0038+8447	00:38:11.86078	+84:47:27.15210	194.02	19.50	0.748	XS

Note. Column (1): J2000 name. Column (2): right ascension for the epoch J2000.0. Column (3): decl. for the epoch J2000.0. Column (4): error in R.A. in milliarcseconds (mas). Column (5): error in decl. in mas. Column (6): correlation between the errors in R.A. and decl. Column (7): frequency bands in which a source was detected and that were used for the astrometric solution: S—2.3 GHz; X—8.6 GHz.

(This table is available in its entirety in machine-readable form.)

rates were applied to the visibilities, and after that the visibilities were averaged over frequency within each individual IF and over time.

Upon the fringe fitting completion, the data were exported to the NASA VLBI analysis software VTD/pSolve.[7,8] That software implements a robust algorithm for estimation of source coordinates, atmospheric path delay in zenith direction, and a clock function for all the stations but the one taken as the reference using X-band and S-band group delays in the presence of a high number of outliers. The procedure is described in full detail by Petrov (2021). The robustness is achieved by exploiting our knowledge of the statistics of both detections and nondetections and the a priori probability of detection derived from the empirical signal-to-noise ratio (S/N) distribution. This approach was also used by the RadioAstron AGN survey (Kovalev et al. 2020b). The residuals of the group delays of detected observations have Gaussian distribution with the second moment of 0.03 and 0.15 ns for X and S bands, respectively, while the residuals of nondetected observations have a uniform distribution within the fringe search window [−4000, +4000] ns. The procedure works both as an estimator of source positions and as a filter of observations where no interferometric signal was detected. Observations with residuals exceeding 4.5 weighted rms σ over all post-fit residuals at S band and 4.0σ at X band are discarded as outliers.

A source is considered detected if the number of its observations used in the solution, i.e., not suppressed, is at least 3. Estimation of the R.A. and the decl. takes two degrees of freedom. If only two observations of a given source passed the filter, the residuals will be zero for any group delays. If two observations of a given source at S band were detected, and therefore their residuals obey the Gaussian distributions with a given second moment, while the third observation was not detected, the probability that its group delay by chance has post-fit residuals less than 4.5σ and as a result was not discarded as an outlier is $4.5 \times 0.15/4000 = 1.7 \times 10^{-4}$. Similar calculations for X band yield the probability of $4 \times 0.03/4000 = 3 \times 10^{-5}$. Since there are three possible combinations of two detected observations and one nondetected for a set of three observations, the probability that at least one of three observations is not detected is three times higher, namely, 5×10^{-4} for S band and 9×10^{-5} for X band. This makes an astrometric solution a very powerful filter.

[7] http://astrogeo.org/vtd/
[8] http://astrogeo.org/psolve/

Since the fringe fitting procedure processed the observations independently, the fringe reference times for the observations of a given scan were slightly different for different baselines, and the closure of the group delay and the phase delay rate was not preserved. Therefore, the baseline-dependent group delays, phase delay rates, and group delay rates were converted to station-based quantities referred to the common scan reference time using least squares and taking one of the stations as a reference. The baseline-dependent group delays were used for astrometric analysis. The station-based group delays and rates were applied to the visibility data, which were then averaged in time and frequency. The averaged visibilities were used for correlated flux density measurements and source structure modeling.

3.2. A Priori Calibration in AIPS and Comparison of the Results

In AIPS, we followed the commonly used procedure of VLBA data calibration. In the global fringe fitting, separate solutions were found for each IF; the minimum S/N for a detection was set to 4. Note that in AIPS the S/N is defined in a slightly different manner than in PIMA; the PIMA S/N is $\sqrt{\pi/2}$ times smaller than the AIPS S/N. Such a low AIPS S/N threshold was chosen because there are many sources near or below the detection limit in our complete sample. A source was treated as detected and the data for it were used in subsequent analysis only if the detection was confirmed by the robust PIMA detection procedure.

The processing of the same data set of 3 days of the VLBA observations in AIPS and PIMA allowed us to compare their outcomes. For strong sources, both packages yield practically the same result. Considering only observations with the calibrated visibility amplitude greater than 1 Jy, we calculated the median ratio of the visibility amplitudes calibrated in AIPS to the amplitudes calibrated in PIMA. It varies from 94.8% to 99.8% for different daily segments and bands. The difference between the calibrated amplitudes of two packages, therefore, does not exceed the typical amplitude calibration uncertainty of VLBI survey data of 5%–10%. For weak sources close to the detection limit, PIMA is more sensitive. AIPS has a known limitation: it cannot process more than one IF unless they are contiguous. Since the frequency allocation of our data was not contiguous owing to astrometry calibration requirements, we had to process the data with AIPS using each IF independently, setting APARM(5) = 0 in the FRING task. Therefore, we lose sensitivity with respect to PIMA that uses all IFs of a given band for a joint solution.

Taking all this into account, we used the data processed in AIPS for imaging and subsequent analysis of those sources, for which hybrid imaging was robust (see Section 3.4). For other sources (mostly weak and/or strongly resolved), we used the data processed in PIMA.

3.3. Absolute Astrometry

Observations of the VLBA North Polar Cap Survey were also used for absolute astrometry. They were processed in a similar way to the VLBA Calibrator Surveys (e.g., Petrov et al. 2008). We refer the reader to that publication, which discusses a general approach, and here we focus on the technique that is specific for the analysis of this campaign.

All dual-band geodetic VLBI data from 24 hr observing sessions from 1980.04.01 through 2020.03.09, in total 6498 experiments, and three observing sessions of this survey were processed in three least-squares runs. The first run used both X- and S-band data from this survey, the second run used only X-band data, and the third run used only S-band data. The number of detected sources from the survey used in these solutions is 108, 117, and 157, respectively. The estimated parameters are split into three categories: global parameters such as station positions, station velocities, and source coordinates; session-wide parameters, such as pole coordinates, UT1 angle, their time derivatives, and nutation angle offsets; and segment-wide parameters, such as clock function and atmospheric path delay in the zenith direction. The segment-wide parameters are modeled with a B-spline with a time span of 1 hr.

For accounting systematic errors, we computed weights in the following way:

$$w = \frac{1}{k \cdot \sqrt{\sigma_g^2 + a^2 + b^2(e)}}, \quad (1)$$

where σ_g is the group delay uncertainty, k is the multiplicative factor, a is the elevation-independent additive weight correction, and b is the elevation-dependent weight correction. We used $k = 1.3$ based on the analysis of the VLBI-Gaia offset (Petrov et al. 2019b). For processing dual-band observations, we used $b(e) = \beta\sqrt{\tau(e_1)^2_{\rm atm,1} + \tau(e_2)^2_{\rm atm,2}}$, where $\tau(e_i)_{\rm i,atm}$ is the atmospheric path delay at the ith station. We used $\beta = 0.02$ in our work. We made trial runs using all geodetic experiments, and they showed that this choice provides the minimum baseline length repeatability.

For processing single-band observations, we computed the ionospheric delay using the Total Electron Contents (TEC) maps from the analysis of the Global Navigation Satellite System (GNSS) observations. Specifically, we used the CODE TEC time series (Schaer 1999)[9] with a resolution of $5^\circ \times 2.5^\circ \times 2$ hr. However, the TEC maps account only partially for the ionospheric path delay owing to the coarseness of their spatial and temporal resolution. In order to account for the contribution of residual ionosphere-driven errors, we used the same approach as we used for processing single-band Long Baseline Array (LBA) observations (Petrov et al. 2019a). We computed variances of the mismodeled contribution of the ionosphere to group delay in zenith direction for both stations of a baseline, $\rm Cov_{11}$ and $\rm Cov_{22}$, as well as their covariances $\rm Cov_{12}$. Then, for each observation, we computed the predicted rms of the mismodeled ionospheric contribution as

$$b^2_{\rm iono}(e) = \gamma(\rm Cov^2_{11}M_1^2(e) - 2Cov_{12}M_1(e)M_2(e) + Cov^2_{22}\,M_2^2(e), \quad (2)$$

where $M_1(e)$ and $M_2(e)$ are the mapping functions of the ionospheric path delay. We used $\gamma = 0.5$ in our analysis and added $b^2_{\rm iono}(e)$ to $b^2(e)$ when processing single-band observations. The additive parameter a was found by an iterative procedure that makes the ratio of the weighted sum of post-fit residuals to their mathematical expectation close to unity.

We analyzed a data set of 86 target sources with more than 10 detections in the NPCS campaign at both S and X bands. We calculated the position differences from the S-band solution with respect to the X/S solution and similarly for the X band. The position differences normalized over the single-band position uncertainties fit to the Gaussian distribution over right ascensions and decl. with the zero mean and the second moment 0.5 for X-band positions, 0.8 for S-band right ascensions, and have a positive bias of +10 mas and second moment 1.0 for S-band declinations. Since the second moment of the distribution of the normalized differences does not exceed 1, we conclude that the formal uncertainties correctly account for ionosphere-driven systematic errors. The decl. bias in the S-band positions was applied in the catalog.

Although a number of sources were observed in other campaigns, we present here the positions derived only from the observations of the NPCS campaign (see Table 2). We also detected four additional sources, which do not belong to our observing sample but lie close to some of the target sources. They were also used in the astrometric solution, and their coordinates are also given in Table 2. The modern positions of the sources can be found in the Radio Fundamental Catalog (RFC),[10] which is updated on a quarterly basis.

3.4. Hybrid Imaging and Issues with Self-calibration of Weak or Resolved Sources

The next stage of data processing was hybrid imaging in Difmap (Shepherd et al. 1994; Shepherd 1997). Before it, bad data points were flagged manually after visual inspection. Hybrid imaging was done by our automatic script, based on the approach developed by Pearson et al. (1994).

A key part of hybrid imaging is self-calibration. However, for a number of sources in our project, the data cannot be self-calibrated. First of all, there are many sources detected at few baselines that do not form a quadrangle or even a triangle, and, consequently, self-calibration for them is impossible. Another significant difficulty is that the phase self-calibration of noisy data, which is the case of a significant fraction of sources in our sample, may lead to a significant artificial increase of the average visibility amplitude and may even generate a spurious source from pure noise (Wilkinson et al. 1988; Martí-Vidal & Marcaide 2008). The stability and the correctness of the phase self-calibration depend mainly on the S/N of the visibilities and on the *uv*-coverage. One can increase the S/N of solutions by increasing the solution time interval. However, if the solution interval is too long, the averaging becomes incoherent, and the resulting amplitude is underestimated (e.g., Martí-Vidal et al. 2010). Therefore, one

[9] Available at ftp://ftp.aiub.unibe.ch/CODE.

[10] Available at http://astrogeo.org/rfc, maintained by Leonid Petrov.

needs to decide which sources are appropriate for hybrid imaging and find the optimal solution interval depending on the data quality. This problem is well known; see, e.g., Cornwell & Fomalont (1999), Section 5.3.

To test the applicability of phase self-calibration, we performed automatic hybrid imaging of each source detected at six or more baselines with different phase self-calibration solution intervals from the correlator integration time (0.5 s for this experiment) to the whole scan duration (about 8 minutes). We analyzed the dependence of different parameters of the resulting maps on the phase self-calibration solution interval. We found that the most informative parameter is the relation between the phase self-calibration solution interval and the intensity in the central pixel of the map. The intensity in the central pixel reflects not only the changes in the peak intensity of the map but also the peak shifts. The examples of such relations are shown in Figure 2.

The shape of the curves like those shown in Figure 2 varies significantly from source to source. However, the sources may be roughly divided into three groups. For strong sources, with a correlated flux density much higher than the detection limit (panel (a) of Figure 2), the effects discussed above are negligible. Self-calibration works perfectly, correcting visibility phase fluctuations and therefore increasing the peak intensity for about 1%, when short solution intervals are used. For weak sources (panel (b)), the situation is radically different. The phase self-calibration with short (∼1 s) solution intervals creates a partly fake signal from the noise. As a result, the intensity in the map center is several times higher than that after self-calibration with solution intervals of about 10 s and longer. In the case of a very weak source (panel (c)), hybrid mapping is completely unstable. Note, however, that for the short solution interval, in case (c), there appears to be a relatively bright compact source in the center of the map, which is inconsistent with the data before self-calibration. These examples show that the phase self-calibration of the VLBI data must be applied carefully when dealing with weak and/or very resolved sources.

We inspected by eye the plots similar to those in Figure 2 at both frequency bands for all the sources detected at baselines formed by four or more antennas, as well as the resulting maps and calibrated visibilities. We have chosen for hybrid imaging the sources for which this procedure is stable and robust. Whether the phase self-calibration is applicable for a source depends on many factors, including the source structure. There are two main characteristics of the visibility data quality of our snapshot observations: the number of independent points in the *uv*-plane, i.e., the number of baselines at which a source is detected, and the median visibility S/N. Here we call the ratio of the amplitude of the visibility at a given baseline coherently averaged over time and frequency to its statistical error a visibility S/N. Our analysis showed that the hybrid imaging is unstable for the sources with a median visibility $S/N < 6$ and detections at less than 15 baselines. If in our observations a source is detected only at 15 baselines or less, while the total number of VLBA baselines is 45, this means that the source is either strongly resolved or very weak with the flux density near the detection limit. We found that the hybrid imaging is also unstable for some sources with better data. For this reason, we decided manually whether to perform hybrid imaging of a source or not. For the sources for which poor data amount and/or quality prevents their imaging, we performed only the flux

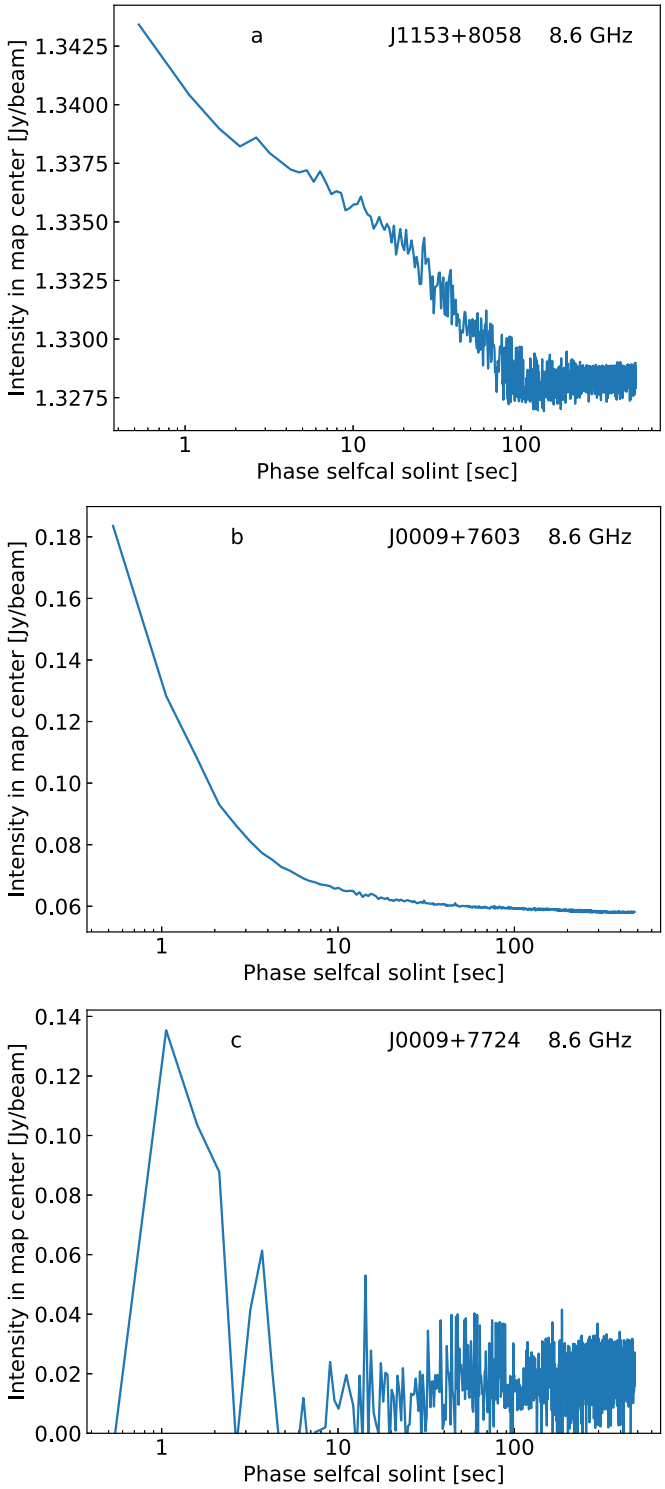

Figure 2. Relation between the intensity in the central pixel of the map, produced by automatic hybrid imaging in Difmap, and the phase self-calibration solution interval used in the procedure. (a) Strong source. (b) Weak source. (c) Very weak source. These plots are shown for the data at 8.6 GHz; at 2.3 GHz the situation is similar. See the discussion in Section 3.4.

density estimation and modeling using the a priori calibrated visibility amplitudes (see Section 4).

For the sources we found suitable for hybrid imaging, we applied a phase self-calibration solution interval of 8 s to avoid the conversion of noise into a signal in the process of phase self-calibration. A longer self-calibration solution interval

limits corrections that compensate short-term phase variations in the atmosphere and might result in a partial incoherence and a loss of the visibility amplitude.

In the process of hybrid imaging, for most of the imaged sources, we also made three iterations of amplitude self-calibration: the first two with one gain correction (per antenna per IF) for the whole scan time, and the third one with a 2-minute solution interval. However, for highly resolved sources, this approach leads to problems. If the correlated flux density sharply decreases with the baseline length at short baselines so that at most baselines it is several times lower than at the shortest one, the CLEAN model cannot fit the data at the shortest baselines. The *uv*-coverage is too poor to allow for a robust model reconstruction. Manipulations with visibility weighting and tapering do not solve the problem. In such situations, the amplitude self-calibration "corrects" visibilities to make them closer to a wrong CLEAN model. Therefore, it significantly changes (usually reduces) visibility amplitude at short spacings. For this reason, we do not apply the amplitude self-calibration to sources for which the ratio of the largest time- and frequency-averaged correlated flux density to the median of averaged correlated flux densities over all baselines is $\geqslant$2.5. There are 21 such sources at 2.3 GHz and 6 sources at 8.6 GHz.

We set a map pixel size of 0.6 mas at 2.3 GHz and 0.15 mas at 8.6 GHz. The default number of pixels was 1024×1024. We also made maps of wider fields using the similar procedure in Difmap to search for outlying components. For the sources in which such components were found, the number of pixels was increased to 2048×2048 or 4096×4096 (the latter for 8.6 GHz only). The bandwidth smearing causes the intensity loss of more than 10% at the distances larger than about 450 mas from the map center in our project. Taking into account that the linear size of the CLEAN map is two times smaller than that of the grid it uses, all our maps cover the area within the radius of 450 mas; therefore, bandwidth smearing is not an issue.

4. Parameters of the Sources Derived from the Visibility Data

From the calibrated visibility data, we obtained a number of parameters that characterize the parsec-scale source structure, in addition to the coordinates and maps of the sources. For the sources for which hybrid imaging was done (Section 3.4), we used self-calibrated visibility data. For the remaining sources, we used the data after a priori calibration only.

First of all, we measured the total flux density of a source $S_{\rm vlba}$ at parsec scales, which we also call the VLBA flux density. We estimated it as the maximum of time- and frequency-averaged correlated flux densities over baseline projections shorter than 10% of the longest VLBA baseline of about 8600 km. If the correlated flux density of a source close to the detection limit changes with the baseline projection nonmonotonically (e.g., for visibility beatings in a double source), the source may be detected only at baseline projections longer than 10% of the longest baseline. In such cases, we took the maximum correlated flux density among all the baselines.

Second, we calculated the median correlated flux density at the baseline projections longer than 70% of the longest VLBA baseline. We call it unresolved flux density $S_{\rm unres}$ because it comes from the features of the source structure practically unresolved by the VLBA. Note, however, that since the *uv*-coverage of our VLBA snapshots is nonisotropic, the measured value of the unresolved flux density depends not only on the source structure but also on the array orientation with respect to a source.

The VLBA flux density for the weakest source detected at 2.3 GHz is 29 mJy, and for the weakest source detected at 8.6 GHz, it is 27 mJy. We conclude that the detection limit of our survey is around 30 mJy for both frequency bands, in agreement with the expected baseline sensitivity of the VLBA for the bandwidth and the integration time of our observations. If there are no detections at long baselines, we put an upper limit on the sources' unresolved flux density. Similarly, if a source is not detected at all, we put an upper limit on its VLBA flux density. In both cases, the upper limit is equal to the detection limit of our observations.

The single-dish observations (Section 6) provided us with the total flux density denoted as $S_{\rm sd}$ from the whole source, including its extended periphery. The ratios of the flux densities from different spatial scales ($S_{\rm unres}$, $S_{\rm vlba}$, and $S_{\rm sd}$) characterize the source compactness. Let us estimate the largest angular scale $\theta_{\rm max}$, for which our VLBA observations are sensitive. The shortest VLBA baseline has a length $D_{\rm max} = 236$ km. Because we observed circumpolar sources, the baseline projections did not differ considerably from their actual length. For 2.3 GHz (wavelength $\lambda = 13$ cm), $\theta_{\rm max} \sim \lambda/D \approx 6 \times 10^{-7}$rad $\approx 0\farcs1$. For the median redshift of the sources in our sample $z_{\rm med} \approx 0.6$ (calculated among the sources with the redshift given in the NED database), it translates to the linear projected size of about 800 pc. Similar calculations for 8.6 GHz ($\lambda = 3.6$ cm) yield a size of about 200 pc. That means that the radiation we observe with the VLBA comes from regions with a characteristic projected size of hundreds of parsecs or smaller. At the same time, the extended extragalactic sources have sizes up to a megaparsec, and the whole source contributes to the total flux density observed by single-dish telescopes. Therefore, the parameter

$$C_{\rm sd}^{\rm vlba} = \frac{S_{\rm vlba}}{S_{\rm sd}} \tag{3}$$

indicates the source compactness at kiloparsec scales, and we call this ratio a kiloparsec-scale compactness parameter. Another ratio,

$$C_{\rm vlba}^{\rm unres} = \frac{S_{\rm unres}}{S_{\rm vlba}}, \tag{4}$$

may be called a parsec-scale compactness parameter because it indicates what fraction of the VLBA flux density comes from the unresolved parsec-scale core. When the VLBA did not detect a source and, hence, only the upper limit on $S_{\rm vlba}$ is known, then for $C_{\rm sd}^{\rm vlba}$ we also can derive an upper limit. A similar situation is for $C_{\rm vlba}^{\rm unres}$ in the case when no detections are available at long projected spacings.

To estimate the size θ and the brightness temperature $T_{\rm b}$ of the main feature of a source, we modeled the source structure in the visibility plane. We used Difmap to fit models of one or two circular Gaussian components to the naturally weighted, self-calibrated complex visibilities. Such simple models were used because of the limited amount of the observational data —only one VLBA scan for each source. Modeling the VLBI data by two circular Gaussians was proven to provide robust results for the dominant feature (e.g., Kovalev et al. 2005;

Pushkarev & Kovalev 2015). We decided which number of components to use by the following method. At first, we fitted one circular Gaussian component and subtracted it from the data. If the peak of the residual map was greater than six times the map rms, we added the second component and refitted the whole model.

For weak or extended sources that were not self-calibrated (see Section 3.4), fitting a model to the complex visibilities may lead to erroneous results owing to incorrect phase values. However, some of these sources have robust detections at a large enough number of baselines to fit a model of one circular Gaussian to the visibility amplitudes only. We did it using the maximum likelihood method with the Rician error distribution.

For practically all the sources modeled by two Gaussians, we consider as "main" the component located closer to the map center, which is typically the position of the intensity peak. However, for several sources detected at both 2.3 and 8.6 GHz, different components dominate in two bands. In such a case, we consider as "main" the component with a flatter spectral index (Hovatta et al. 2014), assuming that we align them properly. The main component may represent physically different structures, depending on the source morphology—a jet core, a mini-lobe, or a compact feature of some extended structure. The flux density of the main Gaussian component $S_{\rm Gauss}$ is, as expected, comparable for most sources to the total VLBA correlated flux density $S_{\rm vlba}$, estimated from the visibility amplitudes at short baselines as described above. The median of the ratio of $S_{\rm Gauss}$ to $S_{\rm vlba}$ is about 0.8 for both frequencies. For strongly resolved sources, $S_{\rm Gauss}$ is slightly higher than $S_{\rm vlba}$ owing to the sharp decrease of the correlated flux density with the increase of the baseline. There are sources for which the decision on the main component identification is based on the spectral index value; their main component at 2.3 GHz accounts for less than half of $S_{\rm vlba}$.

Using the flux density of the main component $S_{\rm Gauss}$ and its FWHM θ, we calculated its brightness temperature in the observer's frame (e.g., Kovalev et al. 2005):

$$T_{\rm b} = \frac{2\ln 2}{\pi k_{\rm B}} \frac{c^2 S_{\rm Gauss}}{\nu^2 \theta^2}, \quad (5)$$

where $k_{\rm B}$ is the Boltzmann constant, c is the speed of light, and ν is the observing frequency. Fitting a model of a circular Gaussian to visibilities of an unresolved source results in an artificially small or zero-size θ, which does not allow us to estimate $T_{\rm b}$ of the component. To avoid this, we calculated the resolution limit $\theta_{\rm lim}$ for the maps of the modeled sources following Lobanov (2005) and Kovalev et al. (2005):

$$\theta_{\rm lim} = b_{\rm maj} \sqrt{\frac{4\ln 2}{\pi} \ln\left(\frac{\rm S/N_{map}}{\rm S/N_{map} - 1}\right)}, \quad (6)$$

where $b_{\rm maj}$ is the major-axis FWHM of the beam and $\rm S/N_{map}$ is the S/N in the image plane in the area occupied by the main component; see Kovalev et al. (2005) for details. If $\theta < \theta_{\rm lim}$, we used $\theta_{\rm lim}$ as the size upper limit and calculated the brightness temperature lower limit $T_{\rm b,lim}$, substituting $\theta_{\rm lim}$ in Equation (5).

Finally, one can calculate the parsec-scale spectral index $\alpha_{\rm vlba}$ from the VLBA flux densities at two frequencies. For the sources detected only in one band, we provide limits on $\alpha_{\rm vlba}$. We note that for some sources there is a problem that leads to biases in $\alpha_{\rm vlba}$ due to the so-called "partial resolution." The shortest baseline at 2.3 GHz corresponds to the spatial frequency being a factor of 3.7 lower than at 8.6 GHz. If the correlated flux density of a source drops significantly between these spatial frequencies, the evaluated spectral index appears to be steeper than the real one. The shorter wavelength of a given interferometer is not sensitive to the emission of extended regions observable at the longer wavelength. This effect is not strong for core-dominated sources since the AGN core size is relatively small and directly proportional to the wavelength (Blandford & Königl 1979). However, this effect can be significant for many sources in our sample.

5. VLBA Survey Results

As a result of this survey, we have detected 162 target sources at any band, 153 sources at 2.3 GHz, 116 sources at 8.6 GHz, and 107 sources at both frequencies. Thus, 32% of the sample of 482 objects have been detected at 2.3 GHz and 24% at 8.6 GHz. The detected sources are those that have a compact feature stronger than the detection limit of the survey, 30 mJy, at the VLBA spatial frequencies, corresponding to angular sizes $\lesssim 0\farcs1$, or linear sizes less than several hundreds of parsecs (see Section 4). Therefore, our fraction of the detected sources is an estimate of the fraction of the sources that have such compact features among all the sources with an NVSS flux density higher than 200 mJy. Under a simplifying assumption that the probability of a source detection in the observed sample does not depend on its total flux density, the probability distribution of this fraction is defined by only two parameters: the total number of sources in the studied sample and the number of detected sources. It allows us to roughly estimate the 1σ confidence intervals for this fraction as [30%; 34%] at 2.3 GHz and [22%; 26%] at 8.6 GHz, using the approach from Cameron (2011), utilizing the quantiles of the beta distribution. This estimate of the confidence intervals is very coarse, since the total flux densities and variability of sources obviously affect the probability distribution of the fraction of sources with strong compact features. To derive this distribution rigorously, a thorough investigation is needed that goes beyond the scope of this work.

The plots of the averaged correlated flux density versus projected baseline (uv radius) for all the detected sources are given in Figure Set 3. We have determined coordinates of all the detected sources with accuracies in the range of 1–100 mas (Table 2). We have restored maps for 94 sources at 2.3 GHz and 62 sources at 8.6 GHz. All the maps and their parameters are given in Figure Set 4. Three sources of the sample (J0017+8135, J1058+8114, and J1153+8058) were also observed as calibrators in all 3 days of the program. For them, we present in Figure Set 3 the plots for each day of our observations separately. We have also restored their maps for each day of our observations.

We have measured the total correlated VLBA flux density for all the detected sources, as described in Section 4. When we had enough data for a source, we also estimated its unresolved flux density, parsec-scale compactness parameter, and VLBA spectral index. These quantities are given in Table 3. We fitted simple models, described in Section 4, to visibilities of 132 sources at 2.3 GHz and 80 sources at 8.6 GHz and obtained the parameters of their dominant components. The angular size of dominant components was measured in both bands for 60 sources; for them, we calculated the power-law index k of the

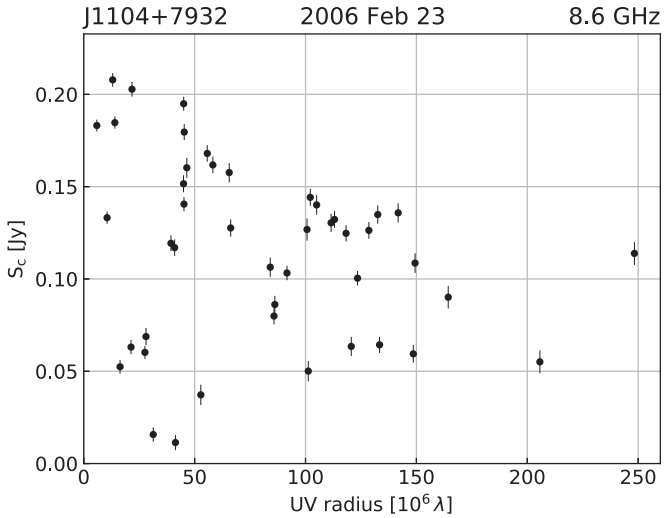

Figure 3. Correlated flux density averaged over time and IFs vs. the *uv* radius for the source J1104+7932 at 8.6 GHz. Similar plots for all the detected sources at 2.3 and/or 8.6 GHz (285 plots) are available. In the cases when the data for a source were calibrated in AIPS and then underwent hybrid imaging in Difmap with both amplitude and phase self-calibration, they are plotted as filled circles. In the cases when the processing was the same except no amplitude self-calibration was made, the data are plotted as filled triangles. In the cases when no self-calibration was made for the source and the data calibrated in PIMA were used, they are plotted as open circles.

(The complete figure set (285 images) is available.)

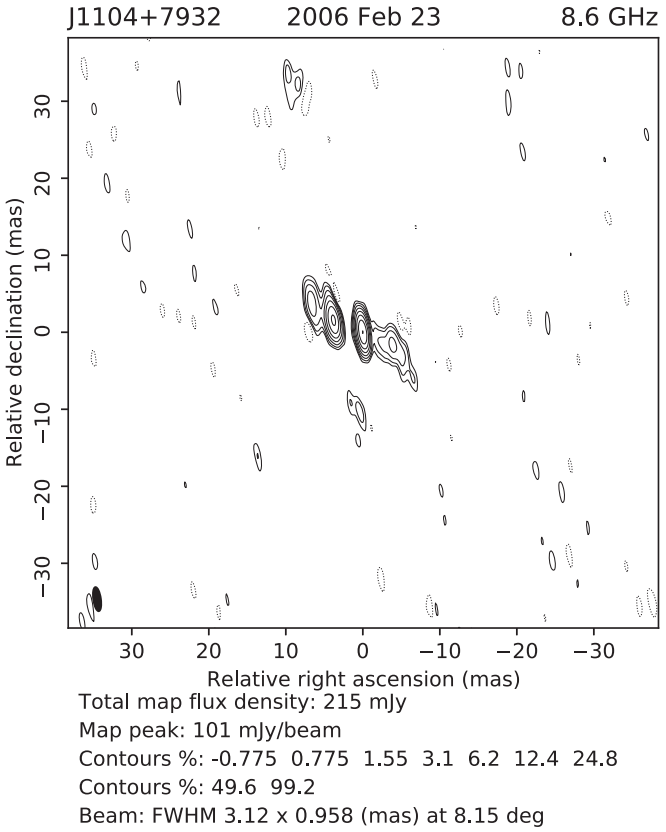

Figure 4. CLEAN map for the source J1104+7932 at 8.6 GHz. The intensity is shown by contours: solid lines are the positive contours, dotted lines are the negative contours. The contour levels in percent of the map peak are specified below the map, as well as the total flux density of the CLEAN model of the source and the intensity of the map peak. First contours correspond to the map noise level × 3; each subsequent contour marks intensity increase by the factor of two. The CLEAN beam at the half-maximum level is shown in the map lower left corner as a black ellipse; its major and minor axes and position angle are specified below the map. All the maps obtained as a result of our survey at both 2.3 and 8.6 GHz (168 images) are available online.

(The complete figure set (168 images) is available.)

angular size–frequency dependence $\theta \propto \nu^{-k}$. These results are given in Table 4. Using VLBA and single-dish flux densities, we also calculated the kiloparsec-scale compactness parameters $C_{\rm sd}^{\rm vlba}$ or their upper limits, which are given in Table 5.

Within this survey framework, we also detected several sources that do not belong to our observing sample but lie close to some of our target sources. We also give the obtained parameters of these sources in Tables 2 and 3, marking them with a flag "ADD" in the latter. We do not use them in the analysis in the subsequent sections, since they do not belong to our complete flux-density-limited sample.

The UVFITS files containing the calibrated visibilities for all the sources detected within this project, the FITS images of all the imaged sources, and the data used for the figures are available online at http://astrogeo.org/npcs/.

6. Total Continuum Radio Spectra

Another type of data we used are the broadband single-dish radio spectra, from which we get total flux densities, spectral indices, and variability amplitudes. We used published spectra, as well as the data from our RATAN-600 observational program. As a result, we have single-dish spectra of all the sample sources at one or several epochs.

For all the sources of our sample, except two closest to the North Celestial Pole, there are published quasi-simultaneous broadband radio spectra (Mingaliev et al. 2007) observed with the RATAN-600—a transit-mode ring radio telescope in the Special Astrophysical Observatory of the Russian Academy of Sciences, located in the North Caucasus (Korolkov & Pariiskii 1979). The sources were observed at the upper culmination with the Southern sector of the telescope at 1.1, 2.3, 4.8, 7.7, and 11.2 GHz; for about one-third of the sources, flux densities at 21.7 GHz were also measured. The observations were carried out in 2005 April–August, i.e., from 10 to 6 months prior to our VLBA observations. The typical accuracy of the flux density measurements is 5%–10%. The telescope has a strongly elongated beam. An essential feature of the RATAN-600 spectra is that they are quasi-simultaneous, i.e., the measurements at all frequencies are made consequently within several minutes. For details see Kovalev et al. (1999) and Botashev et al. (1999).

Our analysis used these spectra for all the sources, except the most extended, which are larger than the RATAN-600 beam. The RATAN-600 does not have the 8.6 GHz receiver, so the flux density at this frequency was estimated from an interpolation. We calculated the single-dish spectral index $\alpha_{\rm sd}$ by fitting a power law to the RATAN-600 flux densities at 2.3, 4.8, and 7.7 GHz. We excluded the measurements that have relative errors larger than 50%.

For the remaining 21 sources, including two closest to the North Celestial Pole and 19 partially resolved by the RATAN-600, we collected all the published nonsimultaneous flux density measurements in the studied frequency range from the CATS database[11] (Verkhodanov et al. 2005) and, neglecting

[11] https://www.sao.ru/cats/

Table 3
VLBA Flux Density and the Compactness Parameters of the Detected Sources

Name (1)	Flag (2)	$S_{\rm vlba,2.3}$ (3)	$S_{\rm unres,2.3}$ (4)	$C^{\rm unres}_{\rm vlba,2.3}$ (5)	$S_{\rm vlba,8.6}$ (6)	$S_{\rm unres,8.6}$ (7)	$C^{\rm unres}_{\rm vlba,8.6}$ (8)	$\alpha_{\rm vlba}$ (9)
J0009+7724	⋯	55±7	⋯	<0.54	51±7	31±6	0.61±0.12	−0.06±0.14
J0009+7603	⋯	49±7	⋯	<0.62	74±9	⋯	<0.40	0.32±0.14
J0013+7748	CSS	403±41	⋯	<0.07	⋯	⋯	⋯	<-1.97
J0017+8135	⋯	861±94	549±56	0.64±0.03	1170±119	699±77	0.60±0.03	0.23±0.11
J0038+8447	CSS	229±23	⋯	<0.13	40±6	⋯	<0.75	−1.32±0.13

Note. Column (1): J2000 source name. Column (2): flag: "CSS" for compact steep-spectrum source candidates; "ADD" for the additional sources not belonging to the target sample detected close to some VLBA pointings. Column (3): VLBA flux density at 2.3 GHz. Column (4): unresolved flux density at 2.3 GHz. Column (5): parsec-scale compactness parameter (ratio of Column (4) to Column (3)) at 2.3 GHz. Column (6): VLBA flux density at 8.6 GHz. Column (7): unresolved flux density at 8.6 GHz. Column (8): parsec-scale compactness parameter at 8.6 GHz. Column (9): VLBA spectral index. Flux density values are given in mJy.

(This table is available in its entirety in machine-readable form.)

Table 4
Results of the Circular Gaussian Model Fitting to the Visibilities

Name (1)	Model(2.3GHz) (2)	$S_{\rm Gauss,2.3}$ (3)	$\theta_{2.3}$ (4)	$T_{\rm b,2.3}$ (5)	Model(8.6GHz) (6)	$S_{\rm Gauss,8.6}$ (7)	$\theta_{8.6}$ (8)	$T_{\rm b,8.6}$ (9)	k (10)
J0009+7724	⋯	⋯	⋯	⋯	3	41 ± 4	0.29	8.0×10^9	⋯
J0009+7603	3	38 ± 4	1.4	4.5×10^9	1	70 ± 7	0.37	8.3×10^9	1.01
J0013+7748	3	464 ± 46	33	1.0×10^8	⋯	⋯	⋯	⋯	⋯
J0017+8135	2	642 ± 64	0.87	2.0×10^{11}	2	676 ± 69	0.19	3.2×10^{11}	1.16
J0038+8447	1	154 ± 16	9.5	3.9×10^8	⋯	⋯	⋯	⋯	⋯

Note. Column (1): J2000 source name. Column (2): model type for 2.3 GHz; the types are: 1—one circular Gaussian; 2—two circular Gaussians; 3—one circular Gaussian fitted to visibility amplitudes only. Column (3): flux density of the main component at 2.3 GHz (mJy). Column (4): FWHM of the main component at 2.3 GHz (mas). Column (5): brightness temperature of the main component at 2.3 GHz (K). Column (6): model type for 8.6 GHz. Column (7): flux density of the main component at 8.6 GHz (mJy). Column (8): FWHM of the main component at 8.6 GHz (mas). Column (9): brightness temperature of the main component at 8.6 GHz (K). Column (10): negative slope of the angular size–frequency dependence for the main component.

(This table is available in its entirety in machine-readable form.)

Table 5
Parameters of Total (Single-dish) Spectra and the Kiloparsec-scale Compactness for All the Sources of Our Sample

Name (1)	$S_{\rm sd,2.3}$ (2)	$S_{\rm sd,8.6}$ (3)	$\alpha_{\rm sd}$ (4)	$\Delta S_{\rm sd,8}$ (5)	V_8 (6)	$C^{\rm vlba}_{\rm sd,2.3}$ (7)	$C^{\rm vlba}_{\rm sd,8.6}$ (8)
J0000+8123	164 ± 56	51 ± 11	-0.86 ± 0.32	⋯	⋯	<0.18	<0.59
J0005+8135	148 ± 22	31 ± 8	-1.15 ± 0.19	⋯	⋯	<0.20	<0.96
J0008+8426	181 ± 27	62 ± 6	-0.86 ± 0.13	⋯	⋯	<0.17	<0.48
J0009+7724	475 ± 30	180 ± 12	-0.74 ± 0.08	13 ± 14	0.04 ± 0.04	0.12 ± 0.02	0.28 ± 0.04
J0009+7603	177 ± 10	110 ± 7	-0.39 ± 0.07	⋯	⋯	0.28 ± 0.04	0.68 ± 0.09

Note. Column (1): J2000 source name. Column (2): single-dish flux density at 2.3 GHz. Column (3): single-dish flux density at 8.6 GHz. Column (4): single-dish spectral index in the 2−8 GHz range. Column (5): variability amplitude of the single-dish flux density at 8 GHz. Column (6): variability index at 8 GHz. Column (7): kiloparsec-scale compactness parameter defined as the ratio of the VLBA flux density to the single-dish flux density at 2.3 GHz, or its upper limit if a source was not detected by VLBA. Column (8): kiloparsec-scale compactness parameter at 8.6 GHz. The unit of the flux density is mJy.

(This table is available in its entirety in machine-readable form.)

the source variability and assuming that the only reason for flux density differences is the partial resolution of the sources, fitted the upper envelopes of the collected spectra by a power law to obtain a single-dish spectral index and flux densities.

The resulting single-dish flux densities and spectral indices are given in Table 5.

We classified the shape of the spectra as follows. Five sources (J0626+8202, J0726+7911, J1044+8054, J1823+7938, and J1935+8130) exhibit a peak in their spectra; they were identified as candidates to gigahertz-peaked spectrum (GPS) sources by Mingaliev et al. (2011). The $S \propto \nu^{+\alpha}$ approximation is not suitable for their spectra; however, for uniformity, we calculate their spectral indices in the same way as for the other sources. We divided the spectra of the other sources into two classes: steep (spectral index $\alpha_{\rm sd} < -0.5$) and flat ($\alpha_{\rm sd} \geqslant -0.5$). The spectral index distribution is presented in Figure 5. The steep-spectrum sources account for 90% of our sample selected at 1.4 GHz, flat-spectrum ones account for 9%, and peaked spectrum ones account for 1%. For optically thin synchrotron sources, there is a steepening of the spectra above a few gigahertz owing to synchrotron cooling (e.g., Carilli et al. 1991). However, it does not bias the flat/steep-spectrum classification.

To investigate the variability of the sources, we supplemented the spectra from Mingaliev et al. (2007) by observations at other epochs. The spectra of 171 sources from the sample with

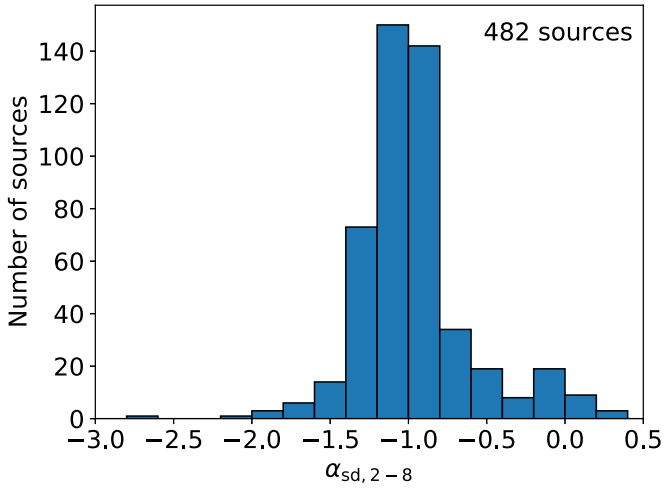

Figure 5. Single-dish 2–8 GHz spectral index distribution for the sources of the sample (see Section 6 for details on the spectral index calculation procedure).

$S_{NVSS} \geqslant 400$ mJy were measured also at the RATAN-600 6 yr earlier (Mingaliev et al. 2001). Furthermore, 37 sources from our sample were observed by Ricci et al. (2013) at 5, 8, 20, and 30 GHz.

Additionally, we used the data from our RATAN-600 AGN monitoring program. The program's description and its results may be found in Kovalev et al. (1999, 2000, 2002, 2020a) and Plavin et al. (2020). In the framework of this program, more than 4000 compact sources were observed at least once, and about 700 sources were monitored for more than a decade. The total broadband 1–22 GHz spectra of more than 95% of the sources were classified by five main types: steep, inverted, super-flat, with a maximum or minimum, and a variable type. They were decomposed into two main spectral components: the first represents the compact jet dominant at higher radio frequencies, and the second one represents an extended magnetoshere around the jet including the far jet region and lobes dominant at frequencies of about 1 GHz and lower. The decomposition of the spectra by two main components has to be valid also for the AGNs in our sample with a detectable parsec-scale structure. However, we note that the steep-spectrum emission at frequencies higher than 1 GHz is attributed, at least partly, to structures of less than about 1 kpc in size; for details see Section 7. Among the sources of our sample, 50 were observed in the framework of our program from 1998 to 2013 with a different number of sets (from 1 to 19 epochs) using the combination of the Flat reflector and the Southern sector of the RATAN-600.

Using all these data, we calculated the variability amplitude of the single-dish flux density for the sources observed at two or more epochs:

$$\Delta S_{sd} = (S - \sigma_S)_{max} - (S + \sigma_S)_{min}, \quad (7)$$

where S and σ_S are the single-dish flux density and its error at a given frequency, and maximum and minimum are calculated over all the epochs. We also calculated the variability index following Aller et al. (1992):

$$V = \frac{(S - \sigma_S)_{max} - (S + \sigma_S)_{min}}{(S - \sigma_S)_{max} + (S + \sigma_S)_{min}}, \quad (8)$$

If the values of the variability amplitude and the variability index, calculated according to Equations (7) and (8), were negative, we set their values to zero. We did not use the flux density measurements of our flux density calibrators in the calculation of the variability parameters. We filtered out measurements with relative errors greater than 1/3 and then inspected the spectra by eye to exclude outliers. The RATAN-600 observations at 2 GHz are often corrupted by man-made radio interference; thus, we did not use variability parameters at this frequency in the analysis. Using the RATAN-600 flux densities at 7.7 GHz from all these programs together with the flux densities from Ricci et al. (2013) at 8.3 GHz, when they were available, we calculated the 8 GHz variability amplitude $\Delta S_{sd,8}$ and variability index V_8 for 167 sources and presented them in Table 5.

7. Analysis

In the previous sections we described our data on the parsec-scale structure and total continuum radio spectra of the sources in our complete sample. Here we present their joint analysis.

7.1. Relation between VLBA Detection and Spectral Index

Figure 6 shows the distribution of the number of detected sources at both VLBA frequencies with respect to the single-dish 2–8 GHz spectral index. The statistics of detections of the sources with different spectrum shapes are summarized in Table 6.

Of flat-spectrum sources, 98% are detected at 2.3 GHz and 95% at 8.6 GHz. That is, our observations of a complete sample verify the common assumption that flat-spectrum sources are compact. At the same time, there are a significant number of detected steep-spectrum sources. The fraction of the detected objects among the steep-spectrum sources is not very high (25% at 2.3 GHz and 16% at 8.6 GHz). However, for our flux-density-limited sample selected at 1.4 GHz, the detected sources with a steep single-dish spectrum outnumber all the flat-spectrum sources. We detected 116 sources with steep single-dish spectra at least in one band, which is 27% of all the sample's steep-spectrum sources. As mentioned in Section 6, there are several GPS sources in our sample, which form a separate class. All of them were detected in both bands.

7.2. Demographics of the Complete Sample

Figure Set 7 shows the single-dish and VLBA broadband spectra for all the sources of the sample. For the sources not detected by the VLBA, upper limits of the VLBA flux density are plotted by arrows.

We can roughly divide steep-spectrum sources into three subclasses:

1. Sources with steep single-dish spectra but flat VLBA spectra. We call them *flat-spectrum cores of extended steep-spectrum sources*. These sources necessarily have rather low kiloparsec-scale compactness, because their total emission is dominated by extended kiloparsec-scale jets and lobes. There are 30 such sources in our sample: 7% of the sources with a steep single-dish spectrum and 6% of the whole complete sample.
2. Sources with both steep single-dish and VLBA spectra. There are 82 such sources in our sample: 19% of steep-spectrum sources and 17% of the whole sample.

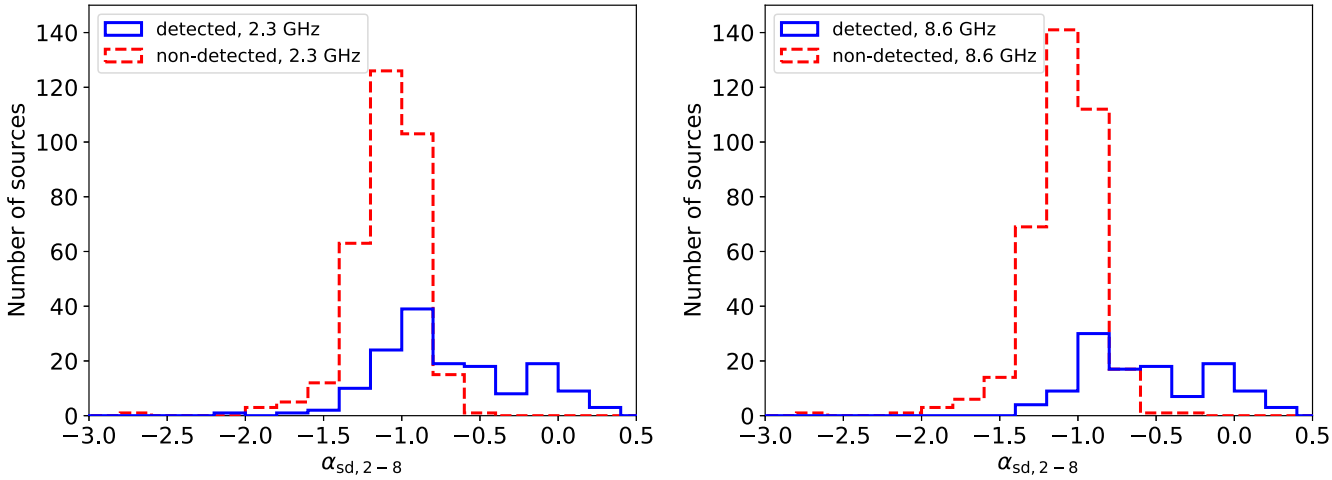

Figure 6. Number of sources in the complete sample detected (solid line) and not detected by the VLBA (dashed line) vs. source single-dish 2–8 GHz spectral index. Left: detections at 2.3 GHz. Right: detections at 8.6 GHz.

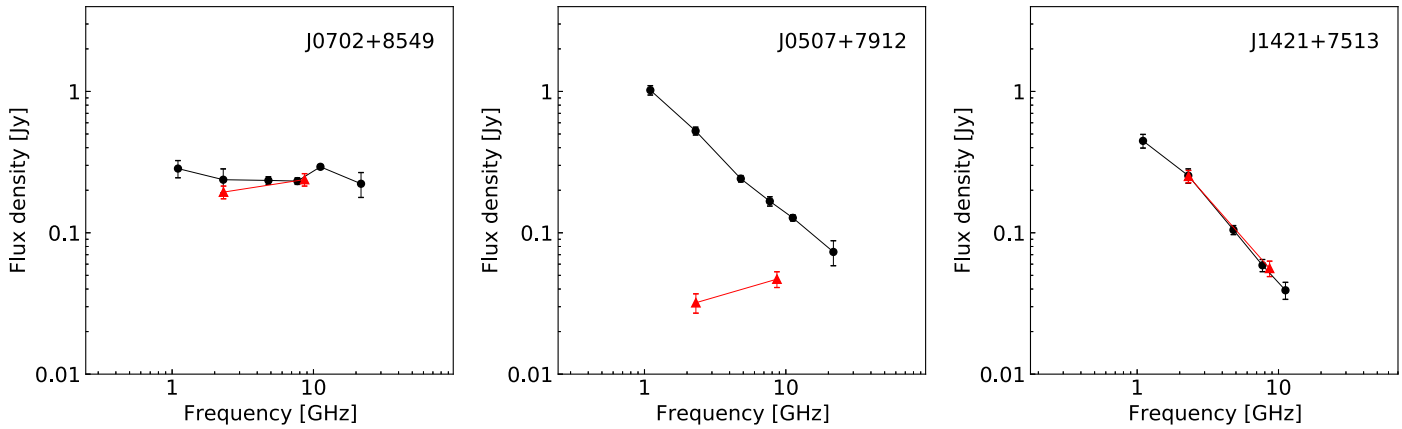

Figure 7. Single-dish and VLBA broadband spectra of all the sources of our sample. The spectra of three sources are shown here as examples. The source name is specified at the top right of each plot. The single-dish spectra are plotted in black; the VLBA spectra are plotted by the red color. In cases of the VLBA nondetection, the upper limits on the VLBA flux density are shown by red arrows.

(The complete figure set (482 images) is available.)

Table 6
Statistics of the VLBA Detections of the Sources in the Complete NVSS Flux-density-limited Sample

Spectral Type (1)	# Sources (2)	# Detected 2.3 GHz (3)	% Detected 2.3 GHz (4)	# Detected 8.6 GHz (5)	% Detected 8.6 GHz (6)
Flat	42	41	98%	40	95%
Steep	435	107	25%	71	16%
Peaked	5	5	100%	5	100%
All	482	153	32%	116	24%

Note. Column (1): type of the continuum single-dish radio spectrum. Column (2): number of sources of a given spectral type in the sample. Column (3): number of sources of a given spectral type detected at 2.3 GHz. Column (4): percent of the detected sources at 2.3 GHz with respect to the number of sources of a given spectral type in the sample. Columns (5) and (6): same as Columns (3) and (4), but for the detections at 8.6 GHz.

3. Extended steep-spectrum sources. This subclass includes all steep-spectrum sources with no detectable parsec-scale structure.

Both the theory (e.g., Blandford & Königl 1979) and the observations (e.g., Hovatta et al. 2014) of AGNs demonstrate that the emission with a flat spectrum is generated in the inner part of relativistic jets close to the central engine. This region is often called the core. It is bright, compact, and located in the place where the synchrotron optical depth is about unity. In our sample, there are 67 sources with $\alpha_{\rm vlba} \geqslant -0.5$, of which 37 sources have a flat single-dish spectrum and 30 sources have a steep single-dish spectrum (type 1 above); here we do not count peaked spectrum sources. Therefore, we observe the opaque core in 14% of the sources in our sample.

If the VLBA spectrum is steep, then some optically thin compact structures dominate the parsec-scale emission rather than the jet core. The objects of the second subclass are most likely CSS sources. A number of them exhibit compact double or compact symmetric morphology in our images, which is typical for CSS sources (see, e.g., O'Dea 1998). We refer to these 82 sources as "CSS candidates," because for most of them we cannot robustly determine the morphology and, thus, cannot say what is detected: a CSS source or just the most compact feature of a hot spot in an extended source. At the same time, 51 of these candidates have $C_{\rm sd}^{\rm vlba} > 0.5$ at 2.3 GHz,

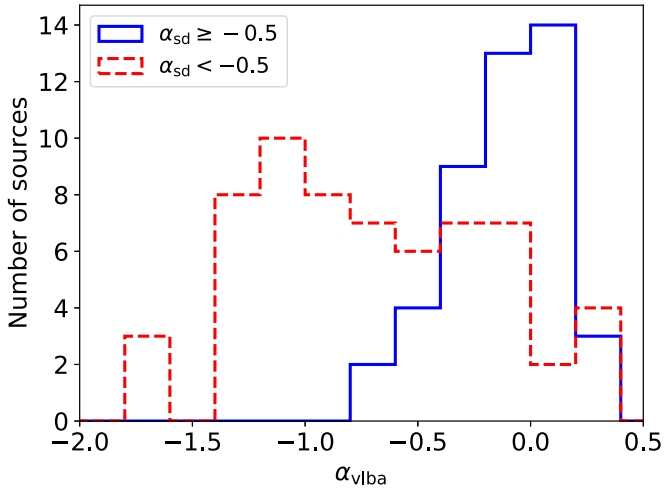

Figure 8. VLBA spectral index histogram for the sources detected in both bands in our survey. The distributions are plotted separately for the sources with a flat single-dish spectrum (solid blue line) and a steep single-dish spectrum (dashed red line).

which indicates that the VLBA detects their features that dominate their integral single-dish flux density. Such sources most likely are CSS. Note that the number of CSS candidates is larger than the number of all flat-spectrum sources in the sample. All 82 CSS candidates are marked by flag "CSS" in Table 3. There are several well-known CSS sources among them, e.g., 0403+768 (J0410+7656), 3C 303.1 (J1443+7707), 3C 305.1 (J1447+7656), and 2342+821 (J2344+8226) (Fanti et al. 1990). Most of them, however, are reported to be VLBI-compact for the first time.

An illustration of the composition of the subpopulation of compact sources within the parent complete NPCS sample is given in Figure 8. There are two histograms in the figure, showing the distributions of the VLBA spectral index for the sources with a flat and a steep single-dish spectrum. Not surprisingly, most of the flat-spectrum sources have a flat spectrum also at parsec scales. For the sources with a steep single-dish spectrum, the broad distribution of α_{vlba} includes sources from both classes 1 and 2. Since CSS sources are more numerous than flat-spectrum cores of extended steep-spectrum sources, the distribution peaks at $\alpha_{vlba} \approx -1$.

7.3. Correlations between Parsec-scale Structure Parameters and Spectral Index

We investigated correlations between the properties of the sources at VLBI spatial scales and their spectral index. In Table 7, we list the Kendall correlation coefficients τ and the probabilities p that the correlation occurred by chance for different pairs of quantities that were defined above. We also indicate the numbers of the sources for which both given quantities are known for each pair. Since for many sources we know upper or lower limits on some parameters instead of their values (see Sections 4 and 5), we calculated the correlation coefficients in two ways: using only measured values and using both measured and censored values (upper and lower limits).

We used the version of the Kendall correlation coefficient known as "tau-b" (Kendall 1945), defined for two variables x_i and y_i (i from 1 to N) as

$$\tau = \frac{\sum_{j=1}^{N}\sum_{i=1}^{j-1} a_{ij} b_{ij}}{\sqrt{(n_0 - n_1)(n_0 - n_2)}}, \quad (9)$$

where $n_0 = N(N-1)/2$, and n_1 and n_2 are the numbers of ties in x and y quantity, correspondingly. In the case when x_i and y_i may be either measured values or upper or lower limits, $a_{ij} = -1$, if x_i is definitely greater than x_j; $a_{ij} = 0$, if $x_i = x_j$ or the comparison of x_i and x_j is uncertain; and $a_{ij} = 1$, if x_i is definitely less than x_j; b_{ij} is defined similarly for y (Brown et al. 1974; Isobe et al. 1986; Akritas & Siebert 1996). We calculated the p-values and the errors of τ, using the expression for the variance of the Kendall correlation statistic from Isobe et al. (1986).

Figure 9 shows the kiloparsec-scale compactness parameter plotted as a function of the single-dish spectral index. Some sources show nonphysical values $C_{sd}^{vlba} > 1$. Besides the measurement errors, it is caused by the source variability since VLBA and single-dish observations were not simultaneous. Since the sample consists of sources with single-dish flux density at 1.4 GHz higher than 200 mJy, the largest possible kiloparsec-scale compactness for a nondetected source at frequency ν with a single-dish spectral index α_{sd} is equal to (detection limit) / [200 mJy $(\nu/1.4\ \mathrm{GHz})^{\alpha_{sd}}$]. This upper envelope is plotted with a gray dashed line.

The kiloparsec-scale compactness (Figure 9) correlates with the single-dish spectral index. The corresponding p-values in Table 7 are very low, especially when the upper limits are taken into account.

In about 90% of the flat-spectrum sources, the emission detected by the VLBA from regions of hundreds of parsecs or less accounts for more than half of the single-dish flux density at both 2.3 and 8.6 GHz. Different steep-spectrum sources have a kiloparsec-scale compactness parameter practically from zero to one. In Figure 9, we mark the type of the VLBA spectrum: flat ($\alpha_{vlba} \geqslant -0.5$) or steep ($\alpha_{vlba} < -0.5$). Several sources for which VLBA spectral type cannot be determined are also indicated. It helps to visually differentiate CSS candidates and flat-spectrum cores of steep-spectrum extended sources.

The parsec-scale compactness parameter C_{vlba}^{unres} has a stronger correlation with α_{vlba} than with α_{sd}. This is a reasonable result: the compactness at a given spatial scale correlates with the spectral index at the same scale. In Figure 10, the parsec-scale compactness is plotted vs. the VLBA spectral index. One can see that the CSS source candidates typically have low parsec-scale compactness, although some of them show high upper limits, especially at 8 GHz, which partially complicates the analysis. The sources with $\alpha_{vlba} \geqslant -0.5$ have C_{vlba}^{unres} in the range from 0 to 1. This scatter is partly due to the sparseness of the uv-coverage of our snapshot observations. Some sources have a beam ellipse eccentricity as low as 0.2. When such a narrow beam is directed perpendicular to a jet, a source is resolved stronger than if the beam ellipse were directed along the jet axis.

The relation between the angular size of the sources and their single-dish spectral index is shown in Figure 11. Note that we could determine sizes not for all the sources of our sample and not for all the VLBA-detected sources but only for those detected at a large enough number of baselines with an acceptable S/N. The upper limits are given for unresolved

Table 7
Kendall Rank Correlation Statistics for Different Pairs of Parameters, Characterizing the Sources Structure and Spectra

Quantities	S Band (2.3 GHz)						X Band (8.6 GHz)					
	Values Only			Values and Limits			Values Only			Values and Limits		
	τ	N	p	τ	N	p	τ	N	p	τ	N	p
$C_{\rm sd}^{\rm vlba}$, $\alpha_{\rm sd}$	0.36 ± 0.05	152	5×10^{-11}	0.27 ± 0.02	481	5×10^{-30}	0.37 ± 0.06	116	7×10^{-9}	0.20 ± 0.02	478	4×10^{-31}
$C_{\rm vlba}^{\rm unres}$, $\alpha_{\rm sd}$	0.27 ± 0.08	82	3×10^{-4}	0.31 ± 0.04	153	3×10^{-13}	0.02 ± 0.09	58	0.84	0.16 ± 0.04	116	1×10^{-4}
$C_{\rm vlba}^{\rm unres}$, $\alpha_{\rm vlba}$	0.37 ± 0.08	82	1×10^{-6}	0.33 ± 0.04	153	6×10^{-17}	0.29 ± 0.09	57	1×10^{-3}	0.20 ± 0.04	116	4×10^{-7}
θ, $\alpha_{\rm sd}$	-0.52 ± 0.06	124	2×10^{-17}	-0.47 ± 0.06	132	1×10^{-15}	-0.40 ± 0.08	67	2×10^{-6}	-0.37 ± 0.07	80	9×10^{-7}
θ, $\alpha_{\rm vlba}$	-0.49 ± 0.07	89	2×10^{-11}	-0.53 ± 0.06	132	3×10^{-21}	-0.47 ± 0.08	67	2×10^{-8}	-0.41 ± 0.07	80	5×10^{-8}
$T_{\rm b}$, $\alpha_{\rm sd}$	0.56 ± 0.06	124	6×10^{-20}	0.51 ± 0.06	132	1×10^{-18}	0.59 ± 0.08	67	1×10^{-12}	0.52 ± 0.07	80	2×10^{-12}
$T_{\rm b}$, $\alpha_{\rm vlba}$	0.44 ± 0.07	89	2×10^{-9}	0.51 ± 0.06	132	2×10^{-20}	0.56 ± 0.08	67	3×10^{-11}	0.48 ± 0.07	80	7×10^{-11}

Note. The meaning of the symbols is as follows: $C_{\rm sd}^{\rm vlba}$—kiloparsec-scale compactness parameter; $C_{\rm vlba}^{\rm unres}$—parsec-scale compactness parameter; θ—angular size of the main compact feature; $T_{\rm b}$—its brightness temperature; $\alpha_{\rm sd}$—single-dish 2–8 GHz spectral index; $\alpha_{\rm vlba}$—VLBA 2–8 GHz spectral index; τ—Kendall correlation coefficient; N—the number of sources for which both quantities in the pair are determined; p—probability that the correlation occurred by chance. Statistics are given for two frequency bands and calculated in two ways: using only measured values, as well as values and limits. See Section 7.3 for details.

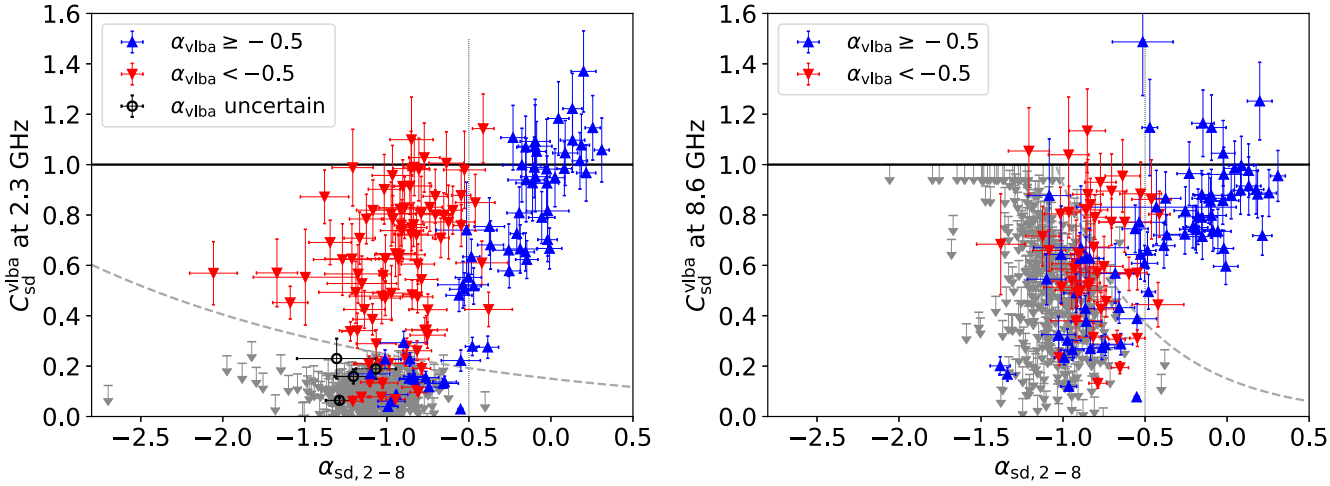

Figure 9. Relation between the kiloparsec-scale compactness parameter $C_{\rm sd}^{\rm vlba}$, defined as the ratio of the VLBA flux density to the total (single-dish) flux density, at two VLBA frequencies and the single-dish 2–8 GHz spectral index $\alpha_{\rm sd,2-8}$. The marker style encodes the type of the VLBA spectrum (see the legend). The upper limits for the sources not detected by the VLBA are marked with gray arrows. The solid line marks the limiting compactness value of 1.0. The dashed line marks the upper envelope of the area, in which nondetected sources could lie (see text for details). The vertical dotted line at $\alpha_{\rm sd} = -0.5$ is the border between steep- and flat-spectrum sources in our terminology.

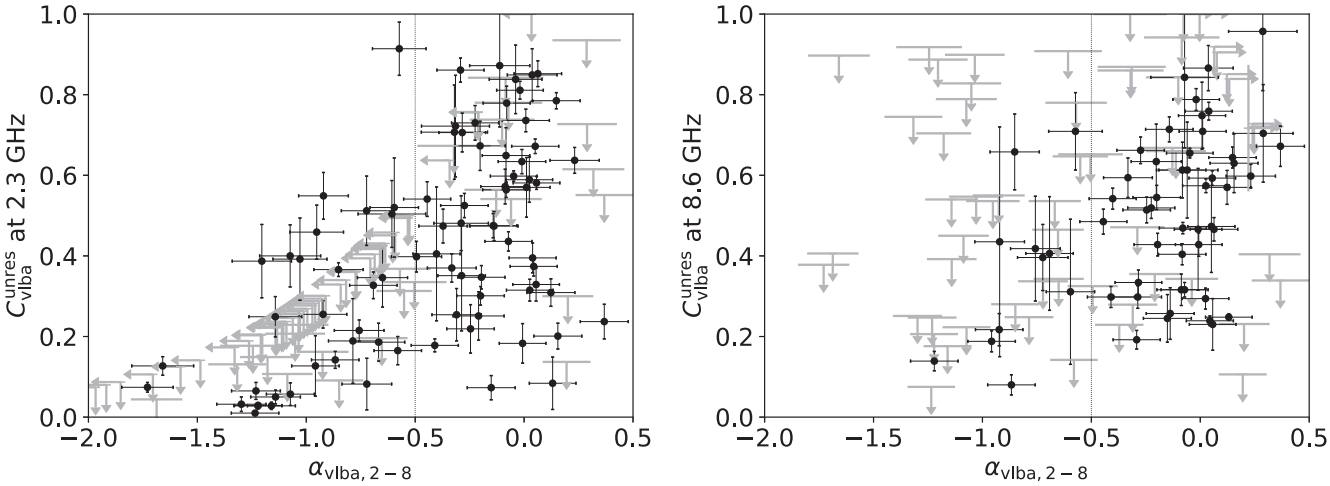

Figure 10. Relation between the parsec-scale compactness parameter $C_{\rm vlba}^{\rm unres}$, defined as the ratio of the unresolved flux density to the VLBA flux density, for two VLBA frequencies and the VLBA spectral index $\alpha_{\rm vlba,2-8}$. The upper limits of compactness for the sources with the VLBA detections only at short baselines and/or upper or lower limits of the VLBA spectral index are marked with gray arrows. Note that less compact sources tend to have steeper spectra.

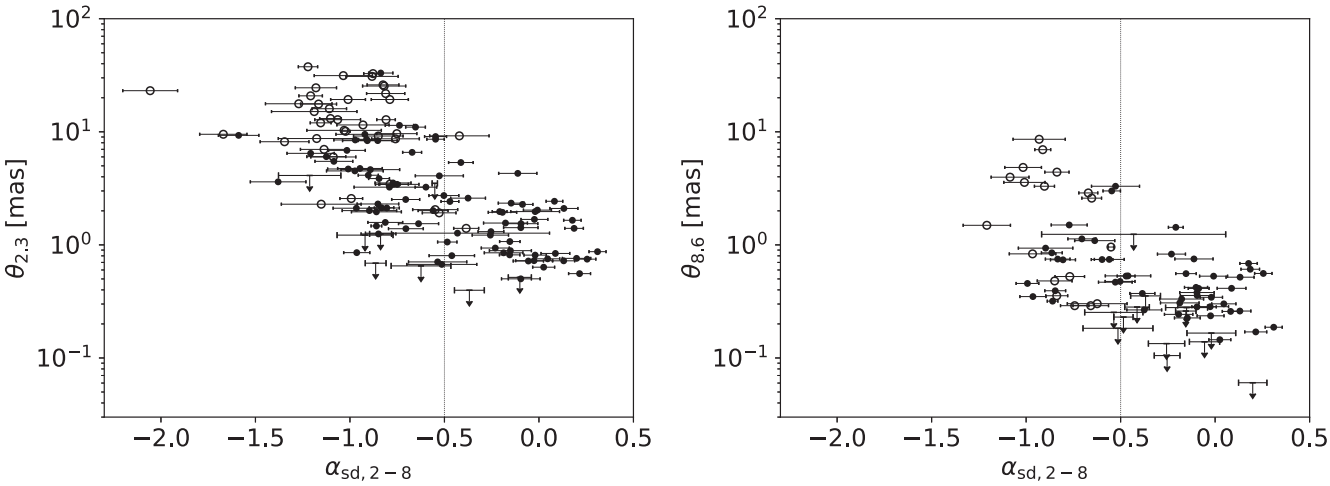

Figure 11. Angular size of the main fitted circular Gaussian component of the sources at 2.3 GHz (left) and 8.6 GHz (right) vs. single-dish 2–8 GHz spectral index. The upper limits are plotted for the unresolved sources. We marked the sizes of components fitted to complex visibilities with filled circles, and those fitted to visibility amplitudes only are marked with open circles (see Section 4 for details). The vertical dotted line divides steep- and flat-spectrum sources.

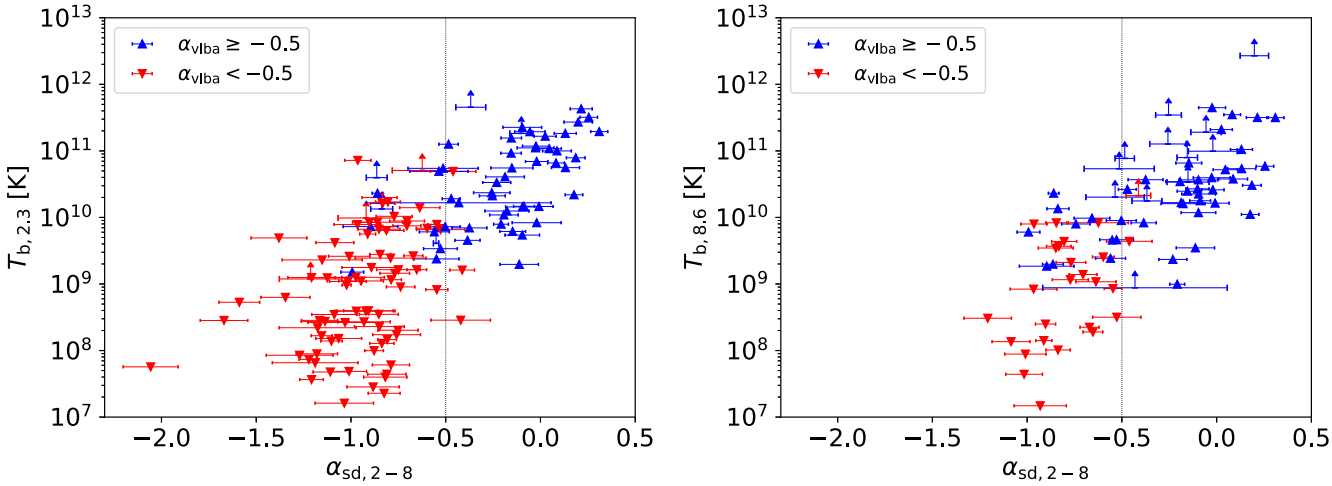

Figure 12. Observer's frame brightness temperature of the main fitted circular Gaussian component of the sources at 2.3 GHz (left) and 8.6 GHz (right) as a function of the single-dish 2–8 GHz spectral index. Symbols are plotted as follows: upward-pointing triangles are the sources with a flat VLBA spectrum, and downward-pointing triangles are the sources with a steep VLBA spectrum.

sources. The formal errors of the fitted parameters are relatively small, about a few percent. We note, however, that they are model dependent, and the formal errors should be treated with a caution. The quantities show a correlation: the flatter is the integral spectrum, the smaller is the dominating feature of the compact structure of a source. In Table 7, the correlation coefficients are given for the angular size θ and the spectral indices $\alpha_{\rm sd}$ and $\alpha_{\rm vlba}$.

Table 7 also shows that the brightness temperature has a significant correlation with the spectral index. Figure 12 shows $T_{\rm b}$ vs. $\alpha_{\rm sd}$. The brightness temperature values are model dependent, and we estimate their accuracy to be of an order of 2. Typically, the steep-spectrum sources have one to two orders of magnitude lower $T_{\rm b}$ than the flat-spectrum ones. However, in Section 7.2 we show that the sources with a steep single-dish spectrum are very different at parsec scales. Figure 12 shows that the flat-spectrum cores of steep-spectrum extended sources have practically the same brightness temperature as their "cousins" with flat single-dish spectra. However, the correlation between the brightness temperature and the spectral index is still present even if we consider only the sources with flat VLBA spectra. In the sources with flat VLBA spectra but steep single-dish spectra, the jet is likely directed at a larger angle to the line of sight than in flat-spectrum sources, which is the reason why the core has lower $T_{\rm b}$ values and does not dominate the total emission. An example of such sources is J1842+7946 (3C 390.3). It has a steep single-dish spectrum and a flat VLBA spectrum. At both frequencies, its kiloparsec-scale compactness is less than 0.1, and its brightness temperature is about 5×10^9 K. Landt et al. (2010) calculated that the jet of this source is directed at 48° to the line of sight. It confirms that the properties of the flat-spectrum cores of extended sources can be explained, at least partly, by a large jet viewing angle.

The CSS candidates have one to two orders of magnitude lower average $T_{\rm b}$ values than the sources with $\alpha_{\rm vlba} \geqslant -0.5$. Together with their steep VLBA spectrum, it indicates that the optically thick jet core does not dominate their emission. VLBI observations with sensitivity and *uv*-coverage better than ours show that the dominating structures of most CSS sources are mini-lobes or jets (Kunert-Bajraszewska et al. 2006; Marecki et al. 2006; Kunert-Bajraszewska & Marecki 2007; Dallacasa et al. 2013). Our results do not contradict that.

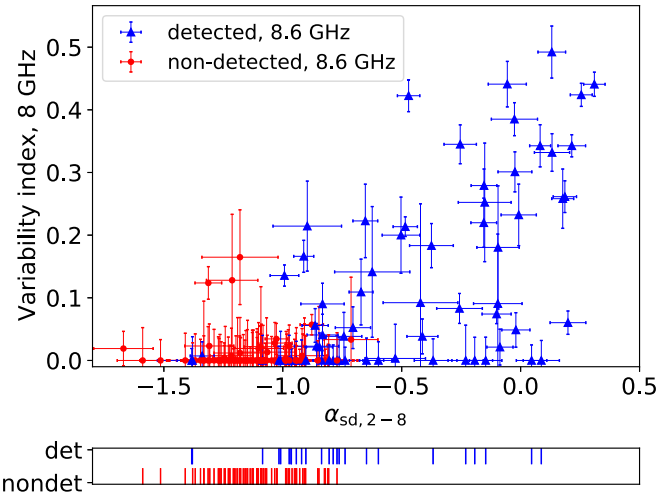

Figure 13. Single-dish flux density variability index at 8 GHz, V_8, vs. instant single-dish 2–8 GHz spectral index for VLBA-detected and nondetected sources. For many of them the variability index is smaller than the measurement errors and is shown as $V_8 = 0$. Spectral index values for the sources with $V_8 = 0$ are marked with vertical lines in the lower panel, for detected and nondetected sources separately.

7.4. Relation between Radio Flux Density Variability and Parsec-scale Structure

We investigated the relation between variability of extragalactic radio sources, inferred from multiepoch single-dish flux density measurements, and their VLBA structure. Our variability data are neither complete nor uniform because single-dish spectra of only a fraction of the sources were observed more than once, and different sources have different numbers of observation epochs. However, keeping this in mind, we are still able to draw useful conclusions from these data.

The variability index at 8 GHz, V_8 (Equation (8)), is shown for the VLBA-detected and nondetected sources in Figure 13 as a function of the 2–8 GHz single-dish spectral index. As expected from causality arguments, practically all the sources with a significant variability are compact enough to be detected by the VLBA. The exceptions are three nondetected steep-spectrum sources with V_8 between 0.1 and 0.2 (namely, J0424

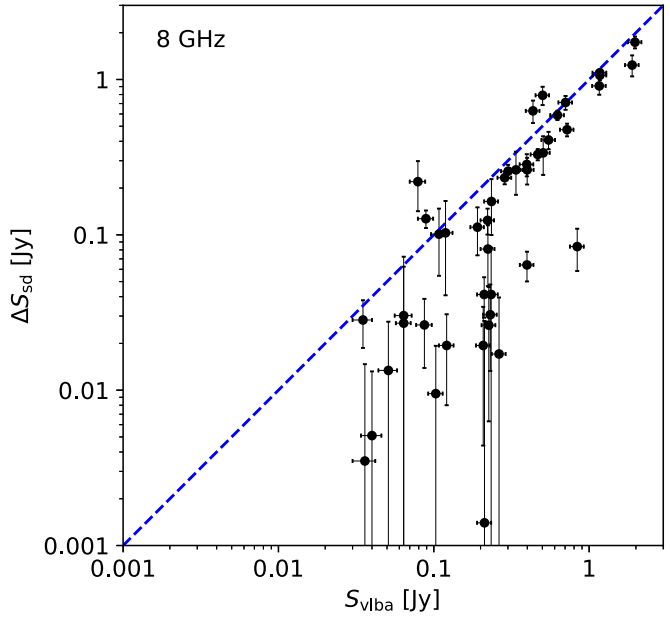

Figure 14. Comparison of the single-dish variability amplitude at 8 GHz and the VLBA flux density at 8.6 GHz for 44 sources with a significant variability. The blue dashed line indicates $\Delta S_{sd} = S_{vlba}$.

+7653, J0920+8628, and J1944+7816). They are rather weak at 8 GHz for RATAN-600 (less than 100 mJy), so their measurement total errors can be underestimated, which causes an overestimated variability index.

Most sources in Figure 13 have a zero variability index, which means that the flux density difference between epochs is less than the measurement errors. To display these sources more clearly, we mark them separately in the lower panel as thin vertical lines at positions equal to their α_{sd}. The detected sources are shown in the upper row, and the nondetected ones are shown in the lower row. Extragalactic sources nondetected by VLBA prevail among the nonvariable objects, which is another sign of the correlation between source variability and the probability of its VLBI detection, i.e., compactness.

Figure 14 shows the variability amplitude of the single-dish flux density (Equation (7)) as a function of the VLBA flux density for 44 variable sources. Most of the points lie close to the blue dashed line, where $\Delta S_{sd} = S_{vlba}$, within their error bars. This means that, indeed, the VLBA-detected components dominate the single-dish flux density variability of the objects. For some sources, the variability amplitude differs significantly from the VLBA flux density. This difference may be due to several reasons. The sources could have been observed by the VLBA in different states of activity. We may have too few epochs of single-dish flux density measurements, and thus the variability amplitude may be underestimated. The VLBA-detected regions could be moderately variable. There are 26 VLBA-detected sources that show no variability exceeding single-dish flux density errors. We conclude that the presence of variability indicates the presence of a compact structure in AGNs (as expected), but the reverse is not true: a significant fraction of compact sources might exhibit weak variability.

A similar trend is shown in Figure 15 in terms of the kiloparsec-scale compactness parameter C_{sd}^{vlba}. Highly variable sources in our sample have large C_{sd}^{vlba} since the compact variable component dominates the total emission for them. At

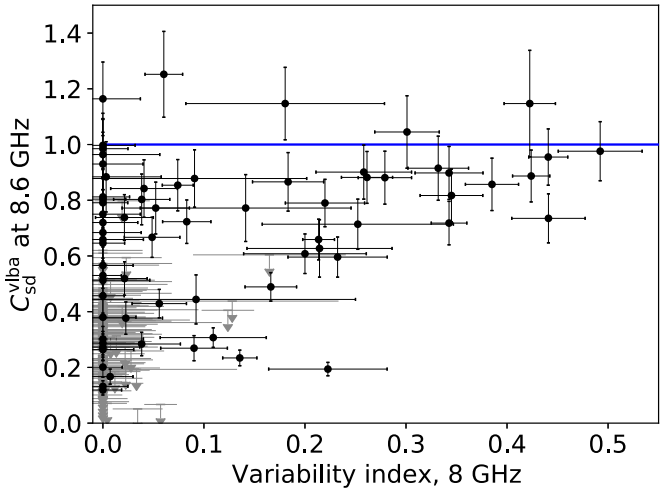

Figure 15. Kiloparsec-scale compactness parameter at 8.6 GHz vs. single-dish variability index at 8 GHz. The blue line marks the maximum compactness value of 1.0. A few points moved above the line owing to the nonsimultaneity of VLBA and single-dish measurements.

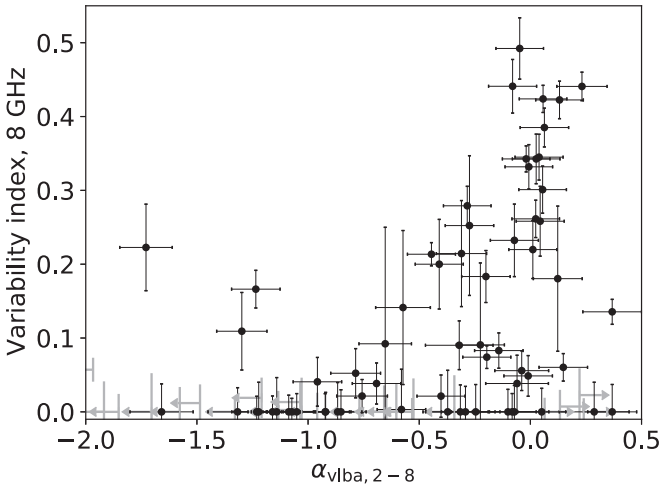

Figure 16. Single-dish variability index at 8 GHz as a function of the VLBA 2–8 GHz spectral index. Note that practically all the sources with significant variability have a flat VLBA spectrum.

the same time, many objects that are very compact at kiloparsec scale show no strong variability.

The information about variability sheds light on the nature of the compact sources with a steep VLBA spectrum. In our sample, such sources are numerous. Figure 16 shows the single-dish 8 GHz variability index vs. the 2–8 GHz VLBA spectral index. All the sources with high variability have a flat spectrum of a compact structure ($\alpha_{vlba} \geqslant -0.5$). Oppositely, most sources with a steep VLBA spectrum have a variability index close to zero. The reason for this dichotomy is that the high variability of emission occurs mostly in the opaque core. If the core dominates the emission, such sources are observed to have flat radio spectra and high variability. Vice versa, if the radio emission is dominated by outer parts of the jet or mini-lobes, we see the combination of a steep spectrum and low variability. Three exceptions from this rule are J1435+7605, J1609+7939, and J2344+8226 (Figure 16). However, their VLBA spectra are measured to be significantly steeper than single-dish spectra. This is unexpected from the general physics picture. Most probably, the VLBA spectral index is underestimated owing to

the effect of partial resolution (see the discussion in Section 4). Another explanation is that the VLBA core of such sources might have the peak of the spectrum at lower radio frequencies.

8. Discussion

Our results show that there are a significant number of steep-spectrum sources with compact features of structure detectable for the VLBI. We observed with the VLBA the complete sample of sources with the total flux density at 1.4 GHz higher than 200 mJy, and we reached the detection limit of 30 mJy. The number of steep-spectrum sources detected at 2.3 GHz is 2.6 times higher than the number of detected flat-spectrum sources. At 8.6 GHz this ratio is 1.8.

The probability that at least one source from the list is falsely detected is 0.01 based on the estimates of the probability of false detection of a given source. It is more difficult to evaluate completeness. We reobserved 283 out of 386 NVSS targets not detected at 8.6 GHz in the NPCS in the framework of the VCS10 observing campaign in 2020. The number of bits at X band collected in that campaign is a factor of 2 greater than in NPCS, and therefore a detection limit is 40% lower. We have detected 13 more sources at 8 GHz. We defer a thorough analysis of the VCS10 until the upcoming publication, but these preliminary results already demonstrate that there is no gross miss of sources above the detection limit.

Using our NPCS detection statistics, we can estimate how many compact sources will be missing in a survey biased toward flat-spectrum sources. The NPCS sample is complete to the level of the VLBA flux density of 200 mJy at 8.6 GHz, not counting the sources with inverted total spectra with $\alpha > 0$. Among the NPCS sources with the VLBA flux density at 8.6 GHz higher than 200 mJy, 33 sources have flat single-dish spectra and 8 sources have steep single-dish spectra. Thus, a catalog with the parent sample of flat-spectrum sources will have a completeness at 200 mJy somewhat higher than 80%. Note that among weaker compact sources steep-spectrum sources dominate, as in our survey with the 30 mJy detection limit; see also Condon & Ledden (1981) and Gorshkov (1991).

The statistics of the sources detections, compactness, and spectral shape depends on the sample selection frequency. In our sample, selected from the NVSS at 1.4 GHz, steep-spectrum sources account for 90%. There were studies of different flux-density-limited samples, selected at higher frequencies (Botashev et al. 1999; Gorshkov et al. 2000, 2003, 2006). In these works, simultaneous broadband radio spectra were observed and analyzed. For a flux density limit similar to ours of 200 mJy, the fraction of the steep-spectrum sources decreases to 57% for the selection frequency 4 GHz, and to 46% for 5 GHz. In the AT20G catalog at 20 GHz, only 27% of the sources have steep spectra at GHz frequencies (Chhetri et al. 2013). Concluding, in the samples selected at higher frequencies, the VLBI detection rate is expected to be higher owing to a higher fraction of the compact flat-spectrum sources. At the same time, the samples selected at lower frequencies are more suitable for studying CSS sources, and they typically go deeper.

Another observational reason for the dependence of the detection statistics on the sample selection frequency and the observing frequency is the following. We selected our sample at 1.4 GHz and observed it at the frequencies several times higher, 2.3 and 8.6 GHz. As a result, we preferably detect, especially at 8.6 GHz, the sources with flatter spectra, since they have a relatively higher flux density at a higher observing frequency. In modern surveys, the detection limit is usually lower, so this limitation is less strict, but it cannot be eliminated completely.

Our results on the relation between the compactness and the spectral index are in a good agreement with earlier works. The percent of CSS sources in our sample is close to that determined by Pearson & Readhead (1988) from a several times smaller sample. Our Figure 9 is similar to Figure 11 in Chhetri et al. (2013): they show the same smooth transition from compact flat-spectrum sources to steep-spectrum sources with the kiloparsec-scale compactness parameter of the latter in the whole range from zero to one. At the same time, there are some differences: the fraction of the extended steep-spectrum sources is much higher in our sample than in the sample of Chhetri et al. (2013), and the flat-spectrum sources are more resolved in our observations. The reasons for that are the higher angular resolution of our observations and the lower selection frequency of our sample.

The angular size–frequency dependence for the compact sources in our sample is in agreement with Pushkarev & Kovalev (2015). This dependence is commonly characterized by a power index k: $\theta \propto \nu^{-k}$. These authors found that for about 2000 extragalactic sources outside the Milky Way plane (galactic latitude $|b| > 10^{\circ}$), the k distribution can be approximated by a Gaussian with a mean of 0.90 and a standard deviation of 0.44. A similar fitting for 60 sources from our sample with sizes measured at both frequencies, 2.3 and 8.6 GHz, yields a peak position at $k = 0.82$ and a standard deviation of 0.51, in agreement with that work.

We identified 82 sources with steep spectra of parsec-scale structure. At the same time, many of them are significantly resolved on parsec scales. Morphology of strongly resolved sources cannot be reliably identified with the VLBI. In such cases, there is a possibility that the VLBA detects only the brightest region in a hot spot of an extended radio galaxy. We call these sources "CSS candidates"; follow-up observations with e-MERLIN and/or VLA are needed to clarify their morphology.

Our detection statistics is based on the fringe amplitude of individual pointed observations of the targets. The calibration converts the fringe amplitude at a given scan and a given baseline to the correlated flux density in Jy. An alternative approach is to image a field where a source is supposed to be located. In such a case a decision about the detection is made on the basis of an excessive surface brightness in Jy beam^{-1} beyond the image noise level. This approach was used in mJIVE-20 (Deller & Middelberg 2014), COSMOS (Herrera Ruiz et al. 2017), and GOODS-N (Radcliffe et al. 2018) VLBI surveys, which have utilized phase referencing for a longer coherent integration and higher sensitivity. For sources that had enough detections to get an image, the total flux density integrated over the image will be the same in both approaches. The case of a source that is partly resolved and detected only at several short baselines is more complicated and requires further investigation. Note that mJIVE-20, COSMOS, and GOODS-N targeted weaker sources than our survey and reported the detection fraction around 20%. The detection fractions of our survey at 2.3 and 8.6 GHz cannot be directly compared with the detection fractions of the mJIVE-20, COSMOS, or GOODS-N at 1.4 GHz. The surveys have used different observing techniques, integration times, and frequencies; their detections and fractions are defined in a different way; and the detection

limit for extended sources is also not equivalent. All these issues are treatable; homogenization of all these surveys is possible. This work will allow us to extend the statistics from the Jy to the 0.1 mJy level.

9. Summary

We have reported the results of the VLBA North Polar Cap Survey—VLBA observations at 2.3 and 8.6 GHz of the large complete flux-density-limited sample drawn from the NVSS catalog *regardless of the spectral index*. Of 482 target sources, 162 were detected. We measured their coordinates and the flux density of compact parsec-scale structure and, for most of the detected sources, the angular size and the brightness temperature of their dominant components. For all the target sources, the total (single-dish) continuum radio spectra were published earlier; for most of them, quasi-simultaneous RATAN-600 spectra at 1–22 GHz are available. This allowed us to analyze the relation between parsec-scale structure and broadband radio spectra. We also characterized single-dish 8 GHz variability for about one-third of the targets using our RATAN-600 AGN monitoring program and the data from the literature.

The VLBA detection statistics shows that a significant fraction of steep-spectrum sources have compact features of a size of several hundreds of parsecs or less. We detected 116 steep-spectrum sources at least in one band compared to 41 detected flat-spectrum sources and 5 peaked spectrum sources. Despite that the detection rate for the latter two spectral types is nearly 100% and for steep-spectrum sources it is only about 25%, steep-spectrum sources account for more than 2/3 of the detected sources because they dominate the full sample selected at 1.4 GHz.

The sources detected by the VLBA and having steep single-dish spectra belong to one of two subclasses. The first one consists of flat-spectrum opaque cores of extended steep-spectrum sources. Their parsec-scale properties are similar to those of the sources with flat single-dish spectra: high compactness, high brightness temperature, and high radio variability. This leads to the conclusion that, together with the flat-spectrum sources, they form a subsample with observable relativistic jet cores. Together they compose 14% of the full sample. The second subclass consists of CSS sources. They have steep spectra at the VLBA spatial scales as well. Their lower parsec-scale compactness and brightness temperature, together with practically no variability in most of them, indicate that their emission comes mostly from optically thin outer parts of jets or mini-lobes. They account for 17% of the full studied sample.

The compactness parameters, the angular size, and the brightness temperature T_b of the sources are correlated with their spectral index: compactness and T_b have a positive correlation, and size has a negative correlation. Our analysis also shows the correlation between the source variability amplitude and its compactness. As expected, the sources variable at 8 GHz are more likely VLBI detectable. The single-dish variability amplitude of most variable sources is observed to be close to the flux density of their components detected by the VLBI. At the same time, we detected with VLBI a significant number of sources showing no variability within the margin of errors.

The selection bias toward flat-spectrum sources was lifted in some recent VLBI surveys, such as the VLBI Ecliptic Plane Survey (Shu et al. 2017) and the VLBA Calibrator Surveys 7, 8, and 9 (Petrov 2021). We ran two VLBA follow-up programs at 4.3 and 7.6 GHz targeting all the AT20G sources with the decl. $> -40^\circ$ and all the sources from the GB6 (Gregory et al. 1996) catalog stronger than 70 mJy within $\pm 7.5^\circ$ of the ecliptic band. The programs were completed in 2020, and the results will be published soon.

We thank Alexander Plavin and Alexander Pushkarev for helpful discussions and comments, and the anonymous referee and Eduardo Ros for valuable suggestions that have helped to improve the manuscript. This study was supported by the Russian Foundation for Basic Research, grant 19-32-90140. The National Radio Astronomy Observatory is a facility of the National Science Foundation operated under cooperative agreement by Associated Universities, Inc. This research is based on the observations with RATAN-600 of the Special Astrophysical Observatory, Russian Academy of Sciences (SAO RAS). The observations with the SAO RAS telescopes are supported by the Ministry of Science and Higher Education of the Russian Federation. The authors made use of the database CATS (Verkhodanov et al. 2005) of the Special Astrophysical Observatory. This research made use of the NASA/IPAC Extragalactic Database (NED), which is operated by the Jet Propulsion Laboratory, California Institute of Technology, under contract with the National Aeronautics and Space Administration.

Facilities: VLBA, RATAN.

Software: AIPS (Greisen 2003), PIMA (Petrov et al. 2011a), Difmap (Shepherd 1997), astropy (Astropy Collaboration et al. 2013, 2018).

ORCID iDs

A. V. Popkov https://orcid.org/0000-0002-0739-700X
Y. Y. Kovalev https://orcid.org/0000-0001-9303-3263
L. Y. Petrov https://orcid.org/0000-0001-9737-9667
Yu. A. Kovalev https://orcid.org/0000-0002-8017-5665

References

Akritas, M. G., & Siebert, J. 1996, MNRAS, 278, 919
Aller, M. F., Aller, H. D., & Hughes, P. A. 1992, ApJ, 399, 16
Astropy Collaboration, Price-Whelan, A. M., Sipőcz, B. M., et al. 2018, AJ, 156, 123
Astropy Collaboration, Robitaille, T. P., Tollerud, E. J., et al. 2013, A&A, 558, A33
Beasley, A. J., Gordon, D., Peck, A. B., et al. 2002, ApJS, 141, 13
Blandford, R. D., & Königl, A. 1979, ApJ, 232, 34
Botashev, A. M., Gorshkov, A. G., Konnikova, V. K., & Mingaliev, M. G. 1999, ARep, 43, 631
Brown, B. W., Hollander, M., & Korwar, R. M. 1974, in Reliability and Biometry: Statistical Analysis of Life Length, ed. F. Prochan & R. J. Serfling (Philadelphia, PA: SIAM), 327
Cameron, E. 2011, PASA, 28, 128
Carilli, C. L., Perley, R. A., Dreher, J. W., & Leahy, J. P. 1991, ApJ, 383, 554
Chhetri, R., Ekers, R. D., Jones, P. A., & Ricci, R. 2013, MNRAS, 434, 956
Collier, J. D., Tingay, S. J., Callingham, J. R., et al. 2018, MNRAS, 477, 578
Condon, J. J., Cotton, W. D., Greisen, E. W., et al. 1998, AJ, 115, 1693
Condon, J. J., Kellermann, K. I., Kimball, A. E., Ivezić, Ž., & Perley, R. A. 2013, ApJ, 768, 37
Condon, J. J., & Ledden, J. E. 1981, AJ, 86, 643
Cornwell, T., & Fomalont, E. B. 1999, in ASP Conf. Ser. 180, Synthesis Imaging in Radio Astronomy II, ed. G. B. Taylor, C. L. Carilli, & R. A. Perley (San Francisco, CA: ASP), 187
Dallacasa, D., Orienti, M., Fanti, C., Fanti, R., & Stanghellini, C. 2013, MNRAS, 433, 147
Deller, A. T., & Middelberg, E. 2014, AJ, 147, 14
Fanti, R., Fanti, C., Schilizzi, R. T., et al. 1990, A&A, 231, 333

Fomalont, E. B., Petrov, L., MacMillan, D. S., Gordon, D., & Ma, C. 2003, AJ, 126, 2562
Giovannini, G., Taylor, G. B., Feretti, L., et al. 2005, ApJ, 618, 635
Gordon, D., Jacobs, C., Beasley, A., et al. 2016, AJ, 151, 154
Gorshkov, A. G. 1991, SvA, 35, 563
Gorshkov, A. G., Konnikova, V. K., & Mingaliev, M. G. 2000, ARep, 44, 353
Gorshkov, A. G., Konnikova, V. K., & Mingaliev, M. G. 2003, ARep, 47, 903
Gorshkov, A. G., Konnikova, V. K., & Mingaliev, M. G. 2006, ARep, 50, 210
Gregory, P. C., Scott, W. K., Douglas, K., & Condon, J. J. 1996, ApJS, 103, 427
Greisen, E. W. 2003, ASSL, 285, 109
Helmboldt, J. F., Taylor, G. B., Tremblay, S., et al. 2007, ApJ, 658, 203
Herrera Ruiz, N., Middelberg, E., Deller, A., et al. 2017, A&A, 607, A132
Hovatta, T., Aller, M. F., Aller, H. D., et al. 2014, AJ, 147, 143
Isobe, T., Feigelson, E. D., & Nelson, P. I. 1986, ApJ, 306, 490
Kellermann, K. I., Condon, J. J., Kimball, A. E., Perley, R. A., & Ivezić, Ž. 2016, ApJ, 831, 168
Kendall, M. G. 1945, Biometrika, 33, 239
Korolkov, D. V., & Pariiskii, I. N. 1979, S&T, 57, 324
Kovalev, Y. A., Kardashev, N. S., Kovalev, Y. Y., et al. 2020a, AdSpR, 65, 745
Kovalev, Y. A., Kovalev, Y. Y., & Nizhelsky, N. A. 2000, PASJ, 52, 1027
Kovalev, Y. Y., Kardashev, N. S., Sokolovsky, K. V., et al. 2020b, AdSpR, 65, 705
Kovalev, Y. Y., Kellermann, K. I., Lister, M. L., et al. 2005, AJ, 130, 2473
Kovalev, Y. Y., Kovalev, Y. A., Nizhelsky, N. A., & Bogdantsov, A. B. 2002, PASA, 19, 83
Kovalev, Y. Y., Nizhelsky, N. A., Kovalev, Y. A., et al. 1999, A&AS, 139, 545
Kovalev, Y. Y., Petrov, L., Fomalont, E. B., & Gordon, D. 2007, AJ, 133, 1236
Kunert-Bajraszewska, M., & Marecki, A. 2007, A&A, 469, 437
Kunert-Bajraszewska, M., Marecki, A., & Thomasson, P. 2006, A&A, 450, 945
Landt, H., Buchanan, C. L., & Barmby, P. 2010, MNRAS, 408, 1982
Liuzzo, E., Giovannini, G., Giroletti, M., & Taylor, G. B. 2009, A&A, 505, 509
Lobanov, A. P. 2005, arXiv:astro-ph/0503225
Madore, B., Helou, G., Corwin, H. G., Jr., et al. 1992, in ASP Conf. Ser. 25, Astronomical Data Analysis Software and Systems I, ed. D. M. Worrall, C. Biemesderfer, & J. Barnes (San Fransisco, CA: ASP), 47
Marecki, A., Kunert-Bajraszewska, M., & Spencer, R. E. 2006, A&A, 449, 985
Martí-Vidal, I., & Marcaide, J. M. 2008, A&A, 480, 289
Martí-Vidal, I., Ros, E., Pérez-Torres, M. A., et al. 2010, A&A, 515, A53
Mingaliev, M. G., Sotnikova, Y. V., Bursov, N. N., Kardashev, N. S., & Larionov, M. G. 2007, ARep, 51, 343
Mingaliev, M. G., Sotnikova, Y. V., Larionov, M. G., & Erkenov, A. K. 2011, ARep, 55, 187
Mingaliev, M. G., Stolyarov, V. A., Davies, R. D., et al. 2001, A&A, 370, 78
Murphy, T., Sadler, E. M., Ekers, R. D., et al. 2010, MNRAS, 402, 2403
O'Dea, C. P. 1998, PASP, 110, 493
Padovani, P. 2016, A&ARv, 24, 13
Pearson, T. J., & Readhead, A. C. S. 1981, ApJ, 248, 61
Pearson, T. J., & Readhead, A. C. S. 1988, ApJ, 328, 114
Pearson, T. J., Shepherd, M. C., Taylor, G. B., & Myers, S. T. 1994, AAS Meeting, 185, 08.08
Petrov, L. 2021, AJ, 161, 14
Petrov, L., de Witt, A., Sadler, E. M., Phillips, C., & Horiuchi, S. 2019a, MNRAS, 485, 88
Petrov, L., Kovalev, Y. Y., Fomalont, E., & Gordon, D. 2005, AJ, 129, 1163
Petrov, L., Kovalev, Y. Y., Fomalont, E. B., & Gordon, D. 2006, AJ, 131, 1872
Petrov, L., Kovalev, Y. Y., Fomalont, E. B., & Gordon, D. 2008, AJ, 136, 580
Petrov, L., Kovalev, Y. Y., Fomalont, E. B., & Gordon, D. 2011a, AJ, 142, 35
Petrov, L., Kovalev, Y. Y., & Plavin, A. V. 2019b, MNRAS, 482, 3023
Petrov, L., Phillips, C., Bertarini, A., Murphy, T., & Sadler, E. M. 2011b, MNRAS, 414, 2528
Plavin, A., Kovalev, Y. Y., Kovalev, Y. A., & Troitsky, S. 2020, ApJ, 894, 101
Polatidis, A. G., Wilkinson, P. N., Xu, W., et al. 1995, ApJS, 98, 1
Preston, R. A., Morabito, D. D., Williams, J. G., et al. 1985, AJ, 90, 1599
Pushkarev, A. B., & Kovalev, Y. Y. 2012, A&A, 544, A34
Pushkarev, A. B., & Kovalev, Y. Y. 2015, MNRAS, 452, 4274
Radcliffe, J. F., Garrett, M. A., Muxlow, T. W. B., et al. 2018, A&A, 619, A48
Ricci, R., Righini, S., Verma, R., et al. 2013, MNRAS, 435, 2793
Schaer, S. 1999, GGAS, 59, 59
Shepherd, M. C. 1997, in ASP Conf. Ser. 125, Astronomical Data Analysis Software and Systems VI, ed. G. Hunt & H. Payne (San Francisco, CA: ASP), 77
Shepherd, M. C., Pearson, T. J., & Taylor, G. B. 1994, BAAS, 26, 987
Shu, F., Petrov, L., Jiang, W., et al. 2017, ApJS, 230, 13
Taylor, G. B., Vermeulen, R. C., Readhead, A. C. S., et al. 1996, ApJS, 107, 37
Thakkar, D. D., Xu, W., Readhead, A. C. S., et al. 1995, ApJS, 98, 33
Verkhodanov, O. V., Trushkin, S. A., Andernach, H., & Chernenkov, V. N. 2005, BSAO, 58, 118
Wilkinson, P. N., Conway, J., & Biretta, J. 1988, in IAU Symp. 129, The Impact of VLBI on Astrophysics and Geophysics, ed. M. J. Reid & J. M. Moran (Dordrecht: Kluwer), 509
Xu, W., Readhead, A. C. S., Pearson, T. J., Polatidis, A. G., & Wilkinson, P. N. 1995, ApJS, 99, 297